Copyright
by
Alexander Mück
1999

RECOIL-INDUCED RESONANCES FOR VELOCIMETRY OF COLD CESIUM ATOMS

by

ALEXANDER MÜCK

THESIS

Presented to the Faculty of the Graduate School of

The University of Texas at Austin

in Partial Fulfillment

of the Requirements

for the Degree of

MASTER OF ARTS

THE UNIVERSITY OF TEXAS AT AUSTIN

August 1999

RECOIL-INDUCED RESONANCES FOR VELOCIMETRY OF COLD CESIUM ATOMS

APPROVED BY
SUPERVISING COMMITTEE:

Supervisor: _____

_____

For Mom and Dad

Acknowledgments

First of all, I want to thank Mark Raizen. When I did not know much about experimental physics at all and what it means to do research he gave me the chance to work in his lab. Thinking back on his great support and his never ending stream of new ideas I have been very fortunate when he offered me a project for my master thesis. I just enjoyed working for him and in his group.

The other physicists working in Mark Raizen's group are just great people and each of them helped to create the unique atmosphere which made it so much fun to work in this lab. First of all, I had the fortune to work with my girlfriend Nicole Helbig. She carried me through all the ups and downs inside and outside the lab and she was a great help in the daily experimental work. After all, it is the greatest pleasure to work with somebody you love.

Our postdoc Valery Milner always helped me to push things forward and supported my work throughout the time. I always had the feeling that my project was as important to him as his personal ones. Thanks for the great help in running the experiment and for the interesting discussions about physics and life in general.

Daniel Steck supported particularly the theoretical background of my project. It is great to work with somebody who knows the answers to your questions. Furthermore, Dan invested a large amount of time in proofreading

my thesis. Thank you.

Windell Oskay spent a lot of time to support my experiment, too. He did not only all the computer programing for the experiment but also helped me to run it. Furthermore, thanks to Windell and Dan for all the fun we had outside the lab and for not forcing me on your schedule.

I also like to thank the people working on *the other experiment*. Braulio Gutiérrez, Martin Fischer and Todd Meyrath added many little things to the daily lab life, which made this year in Texas a unique experience.

Finally, I want to thank some people outside the lab, who helped to make this thesis possible. First of all, thanks to Max Scheer who began to send students from my home university in Würzburg to UT and still does so. Thanks also to Prof. Dr. Langhoff, Prof. Dr. Böhm and Prof. Dr. Yorke who keep the "Würzburg program" going. Here in Austin, I particularly want to thank Prof. Dr. Fink and Norma Kotz who were a great help, but also all the other nice people we met here and who made Austin a lovely place. Finally, I want to acknowledge the German National Merit Foundation (Studienstiftung des deutschen Volkes) for their financial support.

Austin, August 9, 1999

RECOIL-INDUCED RESONANCES FOR VELOCIMETRY OF COLD CESIUM ATOMS

Alexander Mück, M.A.
The University of Texas at Austin, 1999

Supervisor: Mark G. Raizen

This thesis discusses in detail the experimental realization of recoil-induced resonance measurements on cold cesium atoms. Recoil-induced resonances are potentially useful as a velocimetry technique on cold atoms. We discuss this technique from a theoretical standpoint as well as in the context of our experimental results. The good agreement between theory and experiment obtained earlier by other groups in a near-detuned regime is not fully recovered in our far-detuned measurements.

Table of Contents

Acknowledgments **v**

Abstract **vii**

List of Figures **xi**

Chapter 1. Introduction **1**

Chapter 2. Theory of Cooling and Trapping Atoms **4**
2.1 Interaction of Atoms with Light 4
2.1.1 Dissipative and Dispersive Interactions 5
2.1.2 Optical Pumping and Light Shifts of Zeeman Levels 6
2.2 Doppler Cooling and Optical Molasses 7
2.2.1 Basic Mechanism 7
2.2.2 Doppler Limit 8
2.3 Trapping Atoms: The Magneto-Optic Trap 9
2.4 Sub-Doppler Cooling 10
2.4.1 Sisyphus Effect in the lin$\perp$lin Configuration 11
2.4.2 Unbalanced Radiation Pressure in the $\sigma^+ - \sigma^-$ Configuration 13

Chapter 3. Theory of Recoil-Induced Resonances **16**
3.1 Stimulated Raman Transitions between Motional States 17
3.2 Predictions for Recoil-Induced Resonances 26
3.3 Beyond The Ideal Theory 35
3.3.1 The Laser Fields 35
3.3.2 Multiple States 36
3.3.3 Dynamics 38

Chapter 4. Cold Atoms in the Experiment **40**
4.1 Vacuum Chamber 40
4.2 The MOT Beams 42
4.2.1 Trapping Beams 44
4.2.2 Repump Beam 46
4.3 Realization of the Magnetic Field 46

Chapter 5. Experiments on Recoil-Induced Resonances **48**
5.1 Optical Setup and Alignment 48
5.1.1 Setup 49
5.1.2 Alignment 58
5.2 Electronics 61
5.2.1 Frequency Control Electronics 61
5.2.2 Measurement Electronics 65
5.3 Timing 69
5.3.1 MOT Timing 72
5.3.2 Timing of the Experiment 74
5.3.3 TOF Timing 75
5.4 Analysis 75
5.4.1 Noise and Background Suppression 76
5.4.2 Extracting the Momentum Distribution 78
5.4.3 TOF analysis 82

Chapter 6. Results **85**
6.1 General Remarks 85
6.2 Intensity and Detuning 90
6.2.1 Intensity Variations 90
6.2.2 Detuning Variations 98
6.3 Polarization 99
6.3.1 Different Pump and Probe Polarizations 100
6.3.2 Polarization Spectroscopy 100

Chapter 7. Conclusions **103**

Appendices **107**

Appendix A. Cesium Hyperfine Structure **108**

Appendix B. Acousto-Optic Modulators **110**

Bibliography **113**

Vita **116**

List of Figures

2.1 Zeeman level shifts 9
2.2 Polarization in the lin⊥lin configuration 11
2.3 Mechanism for Sisyphus cooling 12
2.4 Polarization in the σ^+-σ^- configuration 13
2.5 Clebsch-Gordan coefficients for $J = 1 \leftrightarrow J = 2$ transitions . . 14

3.1 The geometry of the experiment 27
3.2 Schematic of recoil-induced resonances 30

4.1 Sketch of the vacuum chamber 41
4.2 Optical setup for the MOT beams 44

5.1 The experimental setup 50
5.2 Electronics for frequency control 62
5.3 The frequency sweep 64
5.4 Electronics for taking data 65
5.5 Schematic of the used photodiode circuits 66
5.6 Schematic of the subtraction circuit 67
5.7 Timing diagram 71
5.8 Raw data 77
5.9 Background signal 78
5.10 Background-free lineshape 79
5.11 Example of a momentum distribution 81
5.12 CCD-pictures of the atomic cloud 82
5.13 Momentum distribution from the time-of-flight analysis 83

6.1 Lineshape at 1.5 GHz det., 0.9 mW pump, 0.03 mW probe . . 91
6.2 Lineshape at 1.5 GHz det., 1.5 mW pump, 0.05 mW probe . . 92
6.3 Lineshape at 1.5 GHz det., 2.25 mW pump, 0.075 mW probe . 92

6.4 Lineshape at 1.5 GHz det., 3 mW pump, 0.1 mW probe 93
6.5 Integrated lineshape 93
6.6 Lineshape at 1.5 GHz det., 9 mW pump, 0.3 mW probe 95
6.7 Lineshape at 1.5 GHz det., 15 mW pump, 0.5 mW probe . . . 95
6.8 Lineshape at 1.5 GHz det., 1.2 mW pump, 0.3 mW probe . . . 97
6.9 Lineshape at 1.5 GHz det., 2.4 mW pump, 0.6 mW probe . . . 97

A.1 Cesium hyperfine structure 109

B.1 Principle of an acousto-optic modulator 111

Chapter 1

Introduction

The demonstration of trapping and cooling of atoms in a magneto-optical trap has led to a wide variety of new experiments in recent years. One example is the observation of recoil-induced resonances, which are spectroscopic resonances that rely only on momentum transfer between photons from an applied laser field and atoms within a cold atomic cloud. The physics of this resonant phenomenon can be described in terms of stimulated Raman transitions between motional states of the atoms.

These recoil-induced resonances are not only interesting as a new physical phenomenon. Because of theoretical considerations it has been predicted that they provide a unique spectroscopic method for velocimetry of cold atoms [1]. The method relies on the fact that the lineshape of a recoil-induced resonance is predicted to be the derivative of the momentum distribution of the atoms that are interacting with the laser fields. In 1993, a group in Paris successfully used recoil-induced resonances to determine the temperature of an atomic cloud released from a magneto-optic trap [2,3].

The potential usefulness of a spectroscopic method to determine the momentum distribution in cold atom physics cannot be overestimated. In our

group's experiments, only time-of-flight measurements have thus far provided a reliable technique for measuring the momentum distribution. However, there are several disadvantages of this technique. First of all, the principal problem is that time-of-flight measurements are destructive, because the atoms have to drift freely for several milliseconds during the measurement. This drift destroys the dense atomic cloud needed for many experiments. Moreover, because of the initial size of the atomic cloud before the free drift, this technique does not provide a pure momentum measurement. Other problems are more technical. For example, the measurement is time-consuming, and the whole experiment relies on a CCD-camera that is not completely reliable. Another technique for velocimetry, the use of velocity selective stimulated Raman transitions, also includes severe restrictions. First of all, it is inherently sequential and therefore slow.

Recoil-induced resonance measurements have the big advantage that they can be expected to allow, in principle, for *in situ* measurements of the momentum distribution. A recoil-induced resonance measurement can be performed in less than a millisecond. Moreover, in a far-detuned, non-resonant regime the method should be non-destructive, in that the effect on the momentum distribution should be insignificant.

This thesis describes the experimental implementation and our investigations of this measurement method on cold cesium atoms, which are produced in a magneto-optic trap. In contrast to earlier measurements [2,3], our beams are far-detuned from resonance (several hundred MHz to several GHz), such that we explore new parameter settings with our experiment. The first part

of the thesis is devoted to the theory underlying our experiments. First, in Chapter 2, we give a short introduction to some theoretical concepts of cold-atom physics. Then, in Chapter 3, we recover the theoretical predictions for our experiments [1–3], based on the theory of stimulated Raman transitions. Chapter 4 briefly describes the experimental realization of a magneto-optic trap needed to provide cold atoms. Then, in Chapter 5, we give a detailed description of the experimental setup for measurements on recoil-induced resonances, which has been built up during the project underlying this thesis. In Chapter 6, we finally turn to our experimental results and compare our measurements with the theoretical predictions obtained before. We describe in detail the observation of recoil-induced resonances at different detunings and different intensities of the laser beams. Furthermore, we investigate the effects of different polarizations and the question of whether recoil-induced resonances can rotate the polarization of a laser beam. We certainly cannot claim that we have reached a non-destructive regime with our measurements. Furthermore, recoil-induced resonances, as observed in our experiments, do not agree as well with the theoretical predictions as, for example, the aforementioned experiments in Paris [2,3]. In Chapter 7, this thesis concludes by summarizing our results, addressing questions that are unanswered by our experiment, and suggesting possible future directions for the investigation of recoil-induced resonances.

Chapter 2

Theory of Cooling and Trapping Atoms

In this chapter we introduce the theory of cooling and trapping atoms. As we will see in Section 3.2, cooling and trapping are both absolutely necessary to prepare initial conditions in the experiment that allow the observation of recoil-induced resonances. We begin with a brief description of the interactions between atoms and light, continue with an explanation of Doppler cooling and trapping and how both mechanisms can be combined to a magneto-optic trap. Finally, we discuss sub-Doppler cooling mechanisms.

2.1 Interaction of Atoms with Light

The key processes that make cooling and trapping of atoms possible are the interactions of the atoms with light. We therefore introduce in this section the different types of interactions as well as some of the effects particularly important for the experiment. For a more detailed description the reader is referred to the book by Cohen-Tannoudji, Dupont-Roc and Grynberg [4].

2.1.1 Dissipative and Dispersive Interactions

Interactions between atoms and light can be divided into two categories: dissipative interactions and dispersive interactions. The former describe the attenuation of a beam governed by the imaginary part of the index of refraction while the latter describe the modification of the speed of light that is described by the real part of the index of refraction.

Dissipative forces, also called radiation pressure forces or scattering forces, are based on the absorption of a photon followed by a spontaneous emission event and are therefore associated with the transfer of momentum from the light to the atom. Photons are emitted in all directions according to a dipole radiation pattern. This leads to a net momentum transfer of $\hbar k$ from the absorbed photon in each spontaneous emission cycle because photons are emitted with equal probability in opposite directions. Furthermore, this process leads to a non zero linewidth of atomic transitions.

The scattering rate Γ' for a cycling transition (where the atom returns to its previous ground state) can be calculated following [4,5]. In the limit $\Omega \ll \Gamma$ or $\Omega \ll |\Delta|$, it is given by

$$\Gamma' = \Omega^2 \frac{\Gamma}{\Gamma^2 + 4\Delta^2}, \tag{2.1}$$

where $\Delta = \omega_{\mathrm{L}} - \omega_{\mathrm{A}}$ is the detuning between the light frequency ω_{L} and the atomic resonance ω_{A}, Ω is the Rabi frequency (which is proportional to the transition dipole moment and the electric field of the light), and Γ is the natural width of the excited state.

Dispersive forces, also called dipole forces or gradient forces, are based on shifts of the atomic energy states due to absorption followed by stimulated

emission of photons. These energy displacements are called light shifts or ac Stark shifts. The atomic energy levels are shifted by $\hbar\omega_{\mathrm{AC}}$ also calculable following Cohen-Tannoudji [4,5] (again in the limit $\Omega \ll \Gamma$ or $\Omega \ll |\Delta|$)

$$\omega_{\mathrm{AC}} = \Omega^2 \frac{\Delta}{\Gamma^2 + 4\Delta^2}. \tag{2.2}$$

Therefore, dispersive forces can be interpreted as the gradient of a position-dependent energy shift $\hbar\omega_{\mathrm{AC}}(\vec{r})$ such that $\vec{F} = -\vec{\nabla}(\hbar\omega_{\mathrm{AC}}(\vec{r}))$.

For large detunings ($|\Delta| \gg \Gamma$), Γ' is proportional to $1/\Delta^2$ and can be made negligible compared to ω_{AC}, which varies as $1/\Delta$. For small detunings ($|\Delta| \ll \Gamma$), ω_{AC} can be made much smaller than Γ'.

2.1.2 Optical Pumping and Light Shifts of Zeeman Levels

Optical pumping is one example of a dissipative effect. It uses resonant, circularly polarized light to excite the atoms and transfer angular momentum from the light to the atom. It relies on the fact that $\Delta m = \pm 1$ for $\sigma^{\pm}$ polarization in each absorption. Because the spontaneous emissions, in general, cannot fully compensate this increase or decrease in the magnetic quantum number there is a preferred direction in the transitions. Consider, for example, the $J_{\mathrm{g}} = \frac{1}{2} \rightarrow J_{\mathrm{e}} = \frac{1}{2}$ transition and σ^+ polarization of the incoming photons. Only an atom in the $m_{\mathrm{g}} = -\frac{1}{2}$ state can absorb a photon and be excited into $m_{\mathrm{e}} = \frac{1}{2}$. After a certain time (lifetime of the excited state) the atom can return into the ground state by spontaneous emission of a π-polarized photon. In this case it ends up in the $m_{\mathrm{g}} = \frac{1}{2}$ sublevel and remains there because no further σ^+ transitions are possible. One can prepare an ensemble with a high degree of spin orientation in the ground state with this method.

Light shifts depend on the transition dipole moments (see Equation (2.2)). Therefore, the light shift for each Zeeman sublevel depends on the polarization of the incident light. Consider again the $J_g = \frac{1}{2} \rightarrow J_e = \frac{1}{2}$ transition. A σ^+ polarized beam can only shift the $m_g = -\frac{1}{2}$ state while σ^- light shifts only the $m_g = +\frac{1}{2}$ state. The Rabi frequencies Ω for the other transitions are zero. For π polarized light, both states are equally shifted.

2.2 Doppler Cooling and Optical Molasses

In this section we introduce an important cooling mechanism, Doppler cooling, and how it results in "optical molasses". We also briefly discuss the limits of Doppler cooling and come back to sub-Doppler cooling mechanisms in Section 2.4.

2.2.1 Basic Mechanism

Doppler cooling relies on an imbalance between two opposite radiation pressure forces to slow atoms down. It is therefore another example of a dissipative effect. As mentioned before, a cycling transition is needed to make use of radiation pressure forces. Doppler cooling is therefore only possible for atoms that provide such a closed cycle.

Two counterpropagating laser beams with the same intensity and the same frequency (slightly red detuned from the cycling transition used, so that $\omega_L < \omega_A$) result in the same radiation pressure force for an atom at rest. The directions of the two forces, however, are opposite so that the net average force is equal to zero. For a moving atom the situation is quite different.

The frequencies of both waves are Doppler shifted, but in opposite directions. The wave counterpropagating to the velocity of the atom is shifted closer to resonance, while the wave propagating in the same direction as the atom is shifted away from the resonance because of the red detuning. The counterpropagating wave therefore exerts a stronger radiation pressure force than the copropagating wave because of stronger absorption closer to resonance. This results in a net force that opposes the atomic velocity. By using three pairs of counterpropagating waves along three orthogonal directions, one can decelerate atoms efficiently in all directions from the background vapor. The large deceleration and the small final velocity confine the atom within the laser light for some time. Thermal atoms constantly enter the region of the laser beams, leading to a rise in the atomic density and the confinement of a large number of atoms. In this case the laser light results in a sea of photons that acts like an exceptionally viscous fluid, and so it is therefore called "optical molasses."

2.2.2 Doppler Limit

From our previous discussion one can see that the radiation pressure force is a directed force only in the time-averaged sense because it relies on different absorption probabilities. Therefore, the movement of the atom can be treated as a partly directed random walk. The random walk component of the motion leads to a gain in momentum that competes with the Doppler cooling. Including both processes, the theory of Doppler cooling predicts an equilibrium temperature given by

$$k_{\mathrm{B}} T_{\mathrm{D}} = \hbar \frac{\Gamma}{2}, \tag{2.3}$$

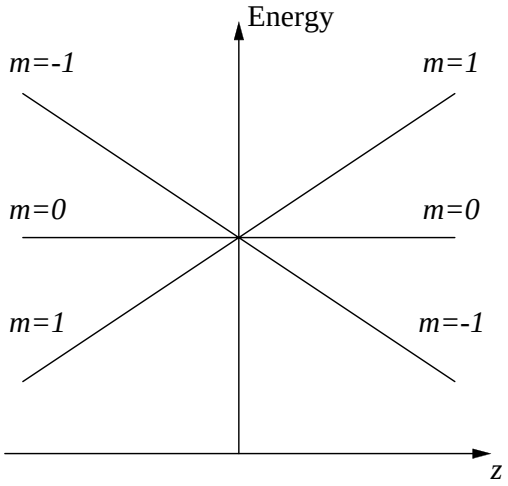

Figure 2.1: Zeeman level shifts in an inhomogeneous magnetic field. The splitting of the levels becomes position dependent and therefore also the detuning from resonance.

where T_{D} is the equilibrium temperature, also called Doppler limit, and Γ is again the natural linewidth of the excited state [5]. This limit is reached for a detuning $\Delta = -\Gamma/2$ and has a value on the order of 100 μK for alkali atoms.

2.3 Trapping Atoms: The Magneto-Optic Trap

At this point we have explained the mechanisms that lead to a cold and slightly confined cloud of atoms. In this section we discuss improvements of the trapping of the atoms, which result in a magneto-optic trap.

To further confine the atoms in space one can apply a magnetic field gradient such that the imbalance between the two radiation pressure forces is position dependent. In a weak inhomogeneous magnetic field $B_z = bz$ the Zeeman sublevels are split by $\Delta E = \mu m B = \mu m b z$. If one illuminates these atoms with two σ^+ and σ^- polarized beams propagating in the $+z$ and

$-z$ directions, respectively, an atom in a certain ground state has different absorption probabilities for σ^+ and σ^- photons. The reason for this effect is that the corresponding Zeeman sublevels of the excited state experience different shifts. For a frequency smaller than the $B = 0$ resonance ($\Delta < 0$), atoms with $z > 0$ will absorb more σ^- photons than σ^+ photons, since the laser frequency is closer to the $\Delta m = -1$ transitions. An atom with $z < 0$ experiences the reversed Zeeman shifts and absorbs more σ^+ than σ^- photons (see Fig. 2.1). In both cases the atom will spontaneously emit a photon in random direction to return to the ground state and therefore experience a net force towards $z = 0$. The $\sigma^+ - \sigma^-$ polarization together with the red detuning preserve all the properties that we discussed for optical molasses in Section 2.2. Therefore, we have preserved the cooling mechanism while adding trapping due to the radiation pressure force, which points towards the point of zero magnetic field. One can extend this scheme to three dimensions and get a so-called "Magneto-Optic Trap" or "MOT".

2.4 Sub-Doppler Cooling

As we have seen in Section 2.2.2, there is a natural limit to cooling using the Doppler shift. Nevertheless, atoms in an optical molasses have been observed to have smaller temperatures (see, for example, [6]). This is due to two different effects, depending on the polarization of the cooling beams. For a lin$\perp$lin configuration the so-called Sisyphus effect comes into play while one gets a radiation pressure imbalance due to motion-induced atomic orientation for $\sigma^+ - \sigma^-$ polarization. We will discuss the Sisyphus effect in Section 2.4.1 and give a qualitative description of the radiation pressure imbalance in Section

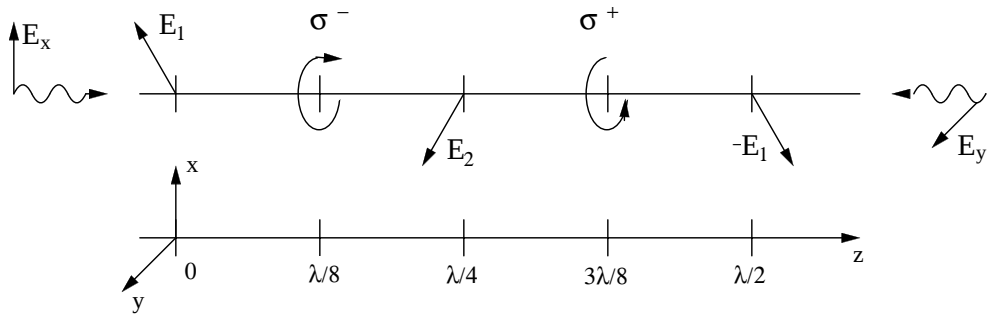

Figure 2.2: Polarization in lin⊥lin configuration. The polarization changes periodically from circular to linear and back.

2.4.2.

2.4.1 Sisyphus Effect in the lin⊥lin Configuration

Sisyphus cooling occurs in a configuration of two counterpropagating beams that are linearly polarized at 90° (lin⊥lin configuration). Beams propagating along the z-axis result in a polarization changing with z as shown in Fig. 2.2. If the light is linearly polarized at $z = 0$, one can conclude that it is circularly polarized at $z = \lambda/8$ and linear but 90° rotated at $z = \lambda/4$ and so on. According to the discussion of the light shifts of Zeeman levels in Section 2.1.2, the energy shifts depend on the polarization and therefore vary periodically with z as well. Consider, for example, a $J = \frac{1}{2} \rightarrow J = \frac{3}{2}$ transition. The $m = +\frac{1}{2}$ sublevel has the largest shift for σ^+ polarized light, while the $m = -\frac{1}{2}$ sublevel has the largest shift for σ^- polarization. Both levels are equally shifted by linearly polarized light (see Fig. 2.3). As discussed previously, for σ^- polarized light the atoms are optically pumped into the $m = -\frac{1}{2}$ ground state and for σ^+ polarization into $m = +\frac{1}{2}$. An atom starting in the $m = -\frac{1}{2}$ ground

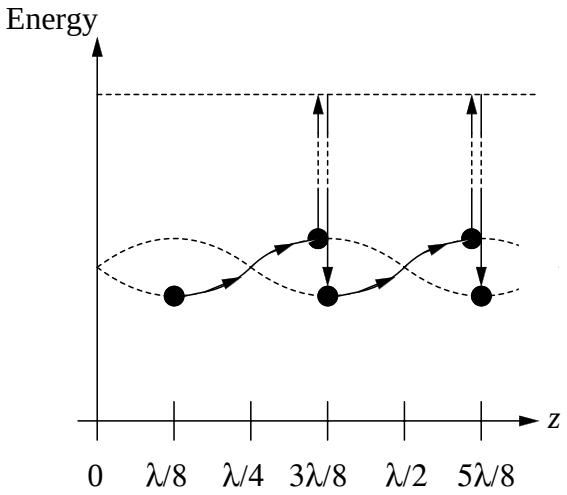

Figure 2.3: Mechanism for Sisyphus cooling. A typical atom will follow the path shown and lose kinetic energy by climbing up the potential hills. The transitions in the opposite direction that lead to an increase in kinetic energy occur with lower probability.

state at a point with σ^- polarization and a non-zero velocity travels towards a point with σ^+ polarization. Since the energy shift of the $m = -\frac{1}{2}$ ground state decreases between these points (the shift is negative and therefore the potential energy increases) the atom has to climb a potential hill. It therefore converts part of its kinetic into potential energy. Before the atom rolls down the hill again the optical pumping, which occurs with a high probability, can lead to a transition into the $m = +\frac{1}{2}$ state. The energy difference between a hill and a valley is then carried away by a spontaneously emitted photon, and the atom is in the $m = +\frac{1}{2}$ state at a position with σ^+ polarization, i.e., in a valley again. Therefore, the same process can repeat itself (see Fig. 2.3). Due to optical pumping, the probability for a transition from the higher energy level to the lower level is less than the probability for the reverse process, so

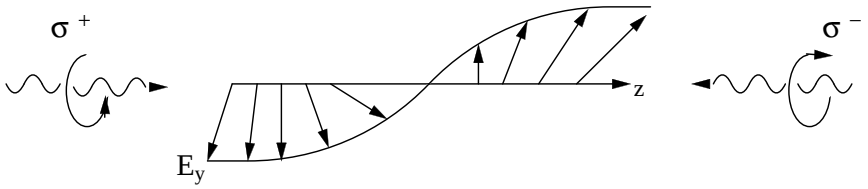

Figure 2.4: Polarization in the σ^+-σ^- configuration.

that on average the atoms climb up more hills than they roll down. Therefore, the combination of varying polarization and optical pumping leads to a cooling of the atoms.

The limit for Sisyphus cooling is reached when the recoil energy due to the spontaneously emitted photon is of the order of the kinetic energy of the atom, and therefore

$$T_{\rm sis} \cong \frac{E_R}{k_{\rm B}}, \tag{2.4}$$

where $E_R = (\hbar k)^2/2M$ is the recoil energy due to the emitted photon. Evaluating this expression results in

$$T_{\rm sis} \approx 0.099\ \mu{\rm K}. \tag{2.5}$$

for cesium atoms.

2.4.2 Unbalanced Radiation Pressure in the $\sigma^+ - \sigma^-$ Configuration

For a $\sigma^+ - \sigma^-$ configuration of the counterpropagating beams the polarization is linear everywhere, but the polarization direction changes with z (see Fig. 2.4). In this case Sisyphus cooling cannot occur. However, for $J_g \geq 1$ there is another process that leads to cooling. We will introduce this process with

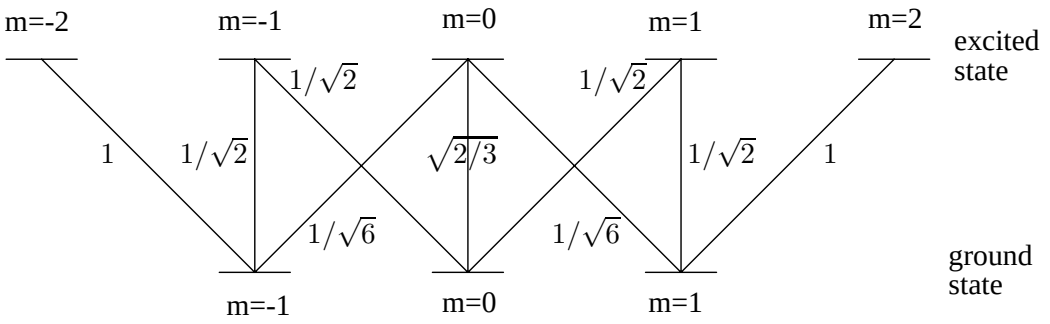

Figure 2.5: Clebsch-Gordan coefficients for $J = 1 \leftrightarrow J = 2$ transitions

the simplest transition, $J_g = 1 \rightarrow J_e = 2$. The Clebsch-Gordan coefficients (i.e., the relative transition amplitudes) for transitions between the different sublevels are shown in Fig. 2.5. The different transition amplitudes result in different light shifts for each of the sublevels. Let us now consider an atom moving with velocity v along the z-axis. It can be shown [8] that transforming the special $\sigma^+ - \sigma^-$ configuration of the laser field in Fig. 2.4 into the atom's rest frame results in an additional potential term

$$V = kvJ_z \tag{2.6}$$

in the Hamiltonian, where k is the absolute value of the wave vector of the light and J_z is the angular momentum operator in the z-direction. Furthermore, one can show that treating this additional term as a perturbation (which is possible for $\Gamma' \ll |\omega'_{\mathrm{AC}}|$ and $kv \ll |\omega'_{\mathrm{AC}}|$) leads to an expectation value for J_z of

$$\langle J_z \rangle = \frac{40}{17} \frac{\hbar k v}{\omega'_{0\mathrm{AC}}}, \tag{2.7}$$

where $\omega'_{0\mathrm{AC}}$ is the light shift of the non-perturbed $m = 0$ ground state. This is equivalent to saying that the $m = \pm 1$ states have different steady-state populations. If the atom is moving in the $+z$-direction ($v > 0$), and we choose red detuning ($\omega'_{0\mathrm{AC}} < 0$), it follows that the difference in population $\Pi_{m=+1} - \Pi_{m=-1} = \langle J_z \rangle / \hbar$ is negative. The opposite is true for an atom moving in the $-z$-direction.

From Fig. 2.5 one sees that for an atom in the $m = -1$ state the probability for absorbing a σ^- photon is six times as high as the one for absorbing a σ^+ photon. The reverse is true for $m = +1$. This difference in absorption probability together with the difference in population of the two $m = \pm 1$ states results in an imbalance between the radiation pressures from the two σ^+ and σ^- waves. The atom on average scatters more counterpropagating than copropagating photons, and its velocity is damped.

Note that the imbalance in the radiation pressure here is not due to the Doppler effect as in Doppler cooling. It results from a population difference in the sublevels of the ground state due to the special configuration of the laser polarizations. This cooling mechanism has a temperature limit much lower than for Doppler cooling. For a detailed description and mathematical derivation of both this effect and Sisyphus cooling see the paper by J. Dalibard and C. Cohen-Tannoudji [8].

Chapter 3

Theory of Recoil-Induced Resonances

In this chapter we introduce the theory of recoil-induced resonances and show that they provide, in principle, an *in situ* temperature measurement method or even more generally a method of velocimetry. Furthermore, we discuss the experimental features necessary to observe recoil-induced resonances.

Recoil-induced resonances are based on stimulated Raman transitions between different motional states of the cesium atoms. In general, a stimulated Raman transition is a two-photon process that couples two different atomic energy levels. One photon is absorbed from a monochromatic light source (usually a laser) and one photon is emitted. In this context, "stimulated" means that the emission is also driven by an external monochromatic field (usually a second laser) as a stimulated process. In recoil-induced resonance experiments these two light sources have to be different (see Section 5.1 for the experimental realization).

In contrast to other processes referred to as stimulated Raman transitions, the atom's internal structure is unchanged. Only the motional states before and after the transition differ. Therefore, in some of the literature recoil-induced resonances are also referred to as stimulated Rayleigh resonances or

optical Compton scattering. Nevertheless, we present here the theoretical approach based on Raman processes.

In Section 3.1 the general theory of Raman transitions between motional states of an atom with two internal levels is introduced. In Section 3.2 we use this theory to discuss the origin of the recoil-induced resonance itself and the predictions for our measurement technique, including the requirements for the experimental setup. Finally, Section 3.3 is dedicated to the discussion of complications in our theoretical analysis.

3.1 Stimulated Raman Transitions between Motional States

In the special case of our experimental setup the Raman transitions are driven by two nearly copropagating laser beams that subtend a small angle α. Nevertheless, we will develop the theory for the generic case of Raman transitions between motional states and use the fact that α is small later in Section 3.2.

The two electric fields of the lasers can be parameterized by their frequencies $\omega_{\mathrm{L1,L2}}$, wave vectors $k_{1,2}$, polarization directions $\hat{\epsilon}_{1,2}$ and amplitudes $E_{1,2}$. The dependence of the overall electric field of both beams on position $\vec{r}$ and time t is given by

$$\vec{E}(\vec{r},t) = \hat{\epsilon}_1 E_1 \cos\left(\vec{k}_1 \cdot \vec{r} - \omega_{\mathrm{L1}} t\right) + \hat{\epsilon}_2 E_2 \cos\left(\vec{k}_2 \cdot \vec{r} - \omega_{\mathrm{L2}} t\right), \tag{3.1}$$

or in its complex form by

$$\begin{aligned} \vec{E}(\vec{r},t) =& \frac{1}{2}\hat{\epsilon}_1 E_1 \left(e^{-i\vec{k}_1\cdot\vec{r}} e^{i\omega_{\mathrm{L1}}t} + e^{i\vec{k}_1\cdot\vec{r}} e^{-i\omega_{\mathrm{L1}}t} \right) \\ &+ \frac{1}{2}\hat{\epsilon}_2 E_2 \left(e^{-i\vec{k}_2\cdot\vec{r}} e^{i\omega_{\mathrm{L2}}t} + e^{i\vec{k}_2\cdot\vec{r}} e^{-i\omega_{\mathrm{L2}}t} \right). \end{aligned} \tag{3.2}$$

Having a mathematical description of the external field, we can begin to describe the dynamics of the atoms. To keep our notation simple we work out the general theory for atoms with a two-level electronic structure and consider more realistic cases in Section 3.3. In Hamiltonian dynamics freely propagating atoms can be described by the Hamiltonian

$$H_0 = \frac{p^2}{2m} + \hbar\omega_{\mathrm{g}}|\mathrm{g}\rangle\langle\mathrm{g}| + \hbar\omega_{\mathrm{e}}|\mathrm{e}\rangle\langle\mathrm{e}|, \tag{3.3}$$

which consists of the external kinetic energy and the internal energy. Here p denotes the momentum operator, m the mass of the atom, $\hbar\omega_{\mathrm{g}}$ the energy of the ground state and $\hbar\omega_{\mathrm{e}}$ the energy of the exited state with respect to some zero energy reference level. $|\mathrm{g}\rangle\langle\mathrm{g}|$ and $|\mathrm{e}\rangle\langle\mathrm{e}|$ are the projection operators on the ground and the excited state respectively. Fixing the energy reference level to be the exited state the free Hamiltonian simplifies to

$$H_0 = \frac{p^2}{2m} - \hbar\omega_{\mathrm{g}}|\mathrm{g}\rangle\langle\mathrm{g}|, \tag{3.4}$$

where $\hbar\omega_{\mathrm{g}}$ now denotes the energy difference between the ground and the excited state.

The interaction of the atoms with the external laser fields can be described by the usual interaction Hamiltonian for an atom-field interaction [4]

$$H_{\mathrm{int}} = -\vec{d}\cdot\vec{E}(\vec{r},t), \tag{3.5}$$

where $\vec{d} = -e\vec{r}$ is the electric dipole operator (the product of the electric charge $e > 0$ and the position operator $\vec{r}$), and $E(\vec{r},t)$ is given by Equation (3.2). For a two-level system this operator can be expressed as

$$\begin{aligned} H_{\mathrm{int}} = -\Big[&|\mathrm{g}\rangle\langle\mathrm{g}|\vec{d}\cdot\vec{E}(\vec{r},t)|\mathrm{g}\rangle\langle\mathrm{g}| \;+\; |\mathrm{e}\rangle\langle\mathrm{e}|\vec{d}\cdot\vec{E}(\vec{r},t)|\mathrm{e}\rangle\langle\mathrm{e}| \\ &+ |\mathrm{g}\rangle\langle\mathrm{g}|\vec{d}\cdot\vec{E}(\vec{r},t)|\mathrm{e}\rangle\langle\mathrm{e}| \;+\; |\mathrm{e}\rangle\langle\mathrm{e}|\vec{d}\cdot\vec{E}(\vec{r},t)|\mathrm{g}\rangle\langle\mathrm{g}|\Big]. \end{aligned} \tag{3.6}$$

The first two terms can be neglected because the matrix elements between two identical states vanish because of a parity selection rule. Therefore, Equation (3.6) reduces to

$$H_{\text{int}} = -\Big[a\langle \text{e}|\vec{d}\cdot\vec{E}(\vec{r},t)|\text{g}\rangle + a^{\dagger}\langle \text{e}|\vec{d}\cdot\vec{E}(\vec{r},t)|\text{g}\rangle\Big], \tag{3.7}$$

where we have defined the annihilation operator $a = |\text{g}\rangle\langle \text{e}|$ and creation operator $a^{\dagger} = |\text{e}\rangle\langle \text{g}|$, and we have chosen the matrix elements to be real. We now invoke the dipole approximation and evaluate the matrix elements at each atomic location while keeping the spatial variation of the electric field outside the matrix element. Then we can write the interaction Hamiltonian as

$$\begin{aligned} H_{\text{int}} = -\Big[&\frac{a+a^{\dagger}}{2}\langle \text{e}|\vec{d}\cdot\hat{\epsilon}_1|\text{g}\rangle E_1\Big(e^{-i\vec{k}_1\cdot\vec{r}}e^{i\omega_{\text{L}1}t} + e^{i\vec{k}_1\cdot\vec{r}}e^{-i\omega_{\text{L}1}t}\Big) \\ &+ \frac{a+a^{\dagger}}{2}\langle \text{e}|\vec{d}\cdot\hat{\epsilon}_2|\text{g}\rangle E_2\Big(e^{-i\vec{k}_2\cdot\vec{r}}e^{i\omega_{\text{L}2}t} + e^{i\vec{k}_2\cdot\vec{r}}e^{-i\omega_{\text{L}2}t}\Big)\Big]. \end{aligned} \tag{3.8}$$

The next step in simplifying the interaction Hamiltonian is to use the rotating-wave approximation. This approximation includes neglecting all terms of the form $ae^{-i\omega_{\text{L}i}t}$ and $a^{\dagger}e^{i\omega_{\text{L}i}t}$ $(i = 1, 2)$, because they correspond to transitions from the excited state to the ground state where a photon is absorbed and transitions from the ground state to the excited state where a photon is emitted, which are both extremely unlikely. This reduces the interaction part of the Hamiltonian to

$$\begin{aligned} H_{\text{int}} = &-\langle \text{e}|\vec{d}\cdot\hat{\epsilon}_1|\text{g}\rangle\frac{E_1}{2}\Big(ae^{-i\vec{k}_1\cdot\vec{r}}e^{i\omega_{\text{L}1}t} + a^{\dagger}e^{i\vec{k}_1\cdot\vec{r}}e^{-i\omega_{\text{L}1}t}\Big) \\ &-\langle \text{e}|\vec{d}\cdot\hat{\epsilon}_2|\text{g}\rangle\frac{E_2}{2}\Big(ae^{-i\vec{k}_2\cdot\vec{r}}e^{i\omega_{\text{L}2}t} + a^{\dagger}e^{i\vec{k}_2\cdot\vec{r}}e^{-i\omega_{\text{L}2}t}\Big). \end{aligned} \tag{3.9}$$

It is quite common to introduce the so-called Rabi-frequency Ω_i defined by

$$\Omega_i = -\frac{\langle \text{e}|\vec{d}\hat{\epsilon}_i|\text{g}\rangle E_i}{\hbar}, \tag{3.10}$$

which we have used before in Chapter 2. This simplifies the notation and reduces the interaction Hamiltonian to

$$\begin{aligned} H_{\text{int}} =& \frac{\hbar\Omega_1}{2}\Big(a e^{-i\vec{k}_1\cdot\vec{r}} e^{i\omega_{\text{L}1}t} + a^\dagger e^{i\vec{k}_1\cdot\vec{r}} e^{-i\omega_{\text{L}1}t}\Big) \\ &+ \frac{\hbar\Omega_2}{2}\Big(a e^{-i\vec{k}_2\cdot\vec{r}} e^{i\omega_{\text{L}2}t} + a^\dagger e^{i\vec{k}_2\cdot\vec{r}} e^{-i\omega_{\text{L}2}t}\Big). \end{aligned} \tag{3.11}$$

The Hamiltonian we wrote down before only includes stimulated interactions with the external field. This means that spontaneous emissions are not accounted for by our previous discussion. However, neglecting spontaneous emission is a good approximation. Assuming far detuning of the lasers from resonance, i.e., $\Delta_{\text{L}1} = \omega_{\text{L}1} - \omega_{\text{g}} \gg \Gamma$ and $\Delta_{\text{L}2} = \omega_{\text{L}2} - \omega_{\text{g}} \gg \Gamma$, where Γ denotes as in Chapter 2 the decay rate of the excited state, their transition rate is suppressed by a factor $(\Delta_{\text{Li}}/\Gamma)^{-2}$ (Section 2.1.1). Therefore, spontaneous emission should not be too important for the Hamiltonian dynamics. We return to the question of indirectly including spontaneous emission below.

Finally, we are able to turn to the discussion of the time evolution of our system. The Hamiltonian $H = H_0 + H_{\text{int}}$ as given in Equations (3.4) and (3.11) is inserted in the equation of motion, i.e., in the Schrödinger equation

$$i\hbar\partial_t|\Psi\rangle = H|\Psi\rangle. \tag{3.12}$$

So far, we have only considered the internal part of the state vector $|\Psi\rangle$. In our two-level model it is given by a normalized linear combination of the ground state $|\text{g}\rangle$ and the excited state $|\text{e}\rangle$. Because the kinetic energy term in the Hamiltonian acts on the motional part of the state vector and the electric field is varying in space, we also have to include the center of mass motion of the atoms. In fact, we are primarily interested in the time evolution of the motional

states. Therefore, the state vector $|\Psi\rangle$ is written as a linear combination of direct products of the internal and motional states. Introducing $|\Psi_{\rm g}\rangle$ and $|\Psi_{\rm e}\rangle$ as the motional states of an atom in the ground and excited level, respectively, we can write $|\Psi\rangle$ as

$$|\Psi\rangle = |\Psi_{\rm g}\rangle|{\rm g}\rangle + |\Psi_{\rm e}\rangle|{\rm e}\rangle, \tag{3.13}$$

where $|{\rm g}\rangle$ and $|{\rm e}\rangle$ are normalized and time independent. In other words, $|\Psi_{\rm g}\rangle$ and $|\Psi_{\rm e}\rangle$ carry all the time dependence of the problem. Inserting Equation (3.13) in the Schrödinger equation, we get

$$\begin{aligned} i\hbar\partial_t(|\Psi_{\rm g}\rangle|{\rm g}\rangle + |\Psi_{\rm e}\rangle|{\rm e}\rangle) = \\ \frac{p^2}{2m}(|\Psi_{\rm g}\rangle|{\rm g}\rangle + |\Psi_{\rm e}\rangle|{\rm e}\rangle) - \hbar\omega_{\rm g}|\Psi_{\rm g}\rangle|{\rm g}\rangle \\ + \frac{\hbar\Omega_1}{2}\Big(e^{-i\vec{k}_1\cdot\vec{r}}e^{i\omega_{\rm L1}t}|\Psi_{\rm e}\rangle|{\rm g}\rangle + e^{i\vec{k}_1\cdot\vec{r}}e^{-i\omega_{\rm L1}t}|\Psi_{\rm g}\rangle|{\rm e}\rangle\Big) \\ + \frac{\hbar\Omega_2}{2}\Big(e^{-i\vec{k}_2\cdot\vec{r}}e^{i\omega_{\rm L2}t}|\Psi_{\rm e}\rangle|{\rm g}\rangle + e^{i\vec{k}_2\cdot\vec{r}}e^{-i\omega_{\rm L2}t}|\Psi_{\rm g}\rangle|{\rm e}\rangle\Big), \end{aligned} \tag{3.14}$$

where we have used the orthogonality of $|{\rm g}\rangle$ and $|{\rm e}\rangle$. Using the linear independence of the internal excited and ground state one can extract the following set of coupled differential equations for the coefficients of $|{\rm g}\rangle$ and $|{\rm e}\rangle$:

$$\begin{aligned} i\hbar\partial_t|\Psi_{\rm g}\rangle &= \frac{p^2}{2m}|\Psi_{\rm g}\rangle - \hbar\omega_{\rm g}|\Psi_{\rm g}\rangle \\ &\quad + \frac{\hbar\Omega_1}{2}e^{-i\vec{k}_1\cdot\vec{r}}e^{i\omega_{\rm L1}t}|\Psi_{\rm e}\rangle + \frac{\hbar\Omega_2}{2}e^{-i\vec{k}_2\cdot\vec{r}}e^{i\omega_{\rm L2}t}|\Psi_{\rm e}\rangle \\ i\hbar\partial_t|\Psi_e\rangle &= \frac{p^2}{2m}|\Psi_{\rm e}\rangle \\ &\quad + \frac{\hbar\Omega_1}{2}e^{i\vec{k}_1\cdot\vec{r}}e^{-i\omega_{\rm L1}t}|\Psi_{\rm g}\rangle + \frac{\hbar\Omega_2}{2}e^{i\vec{k}_2\cdot\vec{r}}e^{-i\omega_{\rm L2}t}|\Psi_{\rm g}\rangle. \end{aligned} \tag{3.15}$$

In order to solve equations like this it is easiest to use state vectors that vary on completely different time scales and absorb variations with optical frequencies as we will see below. Unfortunately, this is not the case for $|\Psi_{\rm g}\rangle$

and $|\Psi_{\rm e}\rangle$. We therefore multiply the first equation with a phase factor $e^{-i\omega_{\rm L1}t}$. This results in

$$\begin{aligned} i\hbar\partial_t e^{-i\omega_{\rm L1}t}|\Psi_{\rm g}\rangle &= \frac{p^2}{2m}e^{-i\omega_{\rm L1}t}|\Psi_{\rm g}\rangle + \hbar\Delta_{\rm L1}e^{-i\omega_{\rm L1}t}|\Psi_{\rm g}\rangle \\ &\quad + \frac{\hbar\Omega_1}{2}e^{-i\vec{k}_1\cdot\vec{r}}|\Psi_{\rm e}\rangle + \frac{\hbar\Omega_2}{2}e^{-i\vec{k}_2\cdot\vec{r}}e^{-i\Delta_\omega t}|\Psi_{\rm e}\rangle \\ i\hbar\partial_t|\Psi_e\rangle &= \frac{p^2}{2m}|\Psi_{\rm e}\rangle \\ &\quad + \frac{\hbar\Omega_1}{2}e^{i\vec{k}_1\cdot\vec{r}}e^{-i\omega_{\rm L1}t}|\Psi_{\rm g}\rangle + \frac{\hbar\Omega_2}{2}e^{i\vec{k}_2\cdot\vec{r}}e^{-i\omega_{\rm L2}t}|\Psi_{\rm g}\rangle, \end{aligned} \tag{3.16}$$

where we have defined the relative detuning of the two lasers $\Delta_\omega = \omega_{\rm L1} - \omega_{\rm L2}$ and used $\Delta_{\rm L1} = \omega_{\rm L1} - \omega_{\rm g}$ and

$$ie^{-i\omega_{\rm L1}t}\hbar\partial_t|\Psi_{\rm g}\rangle = i\hbar\partial_t e^{-i\omega_{\rm L1}t}|\Psi_{\rm g}\rangle - i\hbar\omega_{\rm L1}e^{-i\omega_{\rm L1}t}|\Psi_{\rm g}\rangle. \tag{3.17}$$

Defining $|\tilde{\Psi}_{\rm g}\rangle = e^{-i\omega_{\rm L1}t}|\Psi_{\rm g}\rangle$ and expressing the equations of motions in terms of this new phase-shifted state results in

$$\begin{aligned} i\hbar\partial_t|\tilde{\Psi}_{\rm g}\rangle &= \frac{p^2}{2m}|\tilde{\Psi}_{\rm g}\rangle + \hbar\Delta_{\rm L1}|\tilde{\Psi}_{\rm g}\rangle \\ &\quad + \frac{\hbar\Omega_1}{2}e^{-i\vec{k}_1\cdot\vec{r}}|\Psi_{\rm e}\rangle + \frac{\hbar\Omega_2}{2}e^{-i\vec{k}_2\cdot\vec{r}}e^{-i\Delta_\omega t}|\Psi_{\rm e}\rangle \\ i\hbar\partial_t|\Psi_{\rm e}\rangle &= \frac{p^2}{2m}|\Psi_{\rm e}\rangle + \frac{\hbar\Omega_1}{2}e^{i\vec{k}_1\cdot\vec{r}}|\tilde{\Psi}_{\rm g}\rangle + \frac{\hbar\Omega_2}{2}e^{i\vec{k}_2\cdot\vec{r}}e^{i\Delta_\omega t}|\tilde{\Psi}_{\rm g}\rangle. \end{aligned} \tag{3.18}$$

This is the first step in separating the time scales of the two equations. To complete this separation we have to multiply both equations by another phase factor $e^{i\Delta_{\rm L}t}$, where $\Delta_{\rm L} = (\Delta_{\rm L1} + \Delta_{\rm L2})/2$ is the average detuning of the two lasers. The same steps as before including the definition of the corresponding phase shifted-states lead to

$$\begin{aligned} i\hbar\partial_t|\Psi_{\rm g}\rangle &= \frac{p^2}{2m}|\Psi_{\rm g}\rangle + \hbar(\Delta_{\rm L1} - \Delta_{\rm L})|\Psi_{\rm g}\rangle \\ &\quad + \frac{\hbar\Omega_1}{2}e^{-i\vec{k}_1\cdot\vec{r}}|\Psi_{\rm e}\rangle + \frac{\hbar\Omega_2}{2}e^{-i\vec{k}_2\cdot\vec{r}}e^{-i\Delta_\omega t}|\Psi_{\rm e}\rangle \\ i\hbar\partial_t|\Psi_{\rm e}\rangle &= \frac{p^2}{2m}|\Psi_{\rm e}\rangle - \hbar\Delta_{\rm L}|\Psi_{\rm e}\rangle + \frac{\hbar\Omega_1}{2}e^{i\vec{k}_1\cdot\vec{r}}|\Psi_{\rm g}\rangle + \frac{\hbar\Omega_2}{2}e^{i\vec{k}_2\cdot\vec{r}}e^{i\Delta_\omega t}|\Psi_{\rm g}\rangle, \end{aligned} \tag{3.19}$$

where we have dropped all the tildes to keep our notation simple. Therefore, $|\Psi_g\rangle$ and $|\Psi_e\rangle$ denote now the correctly phase-shifted states.

Now, the time dependencies of the excited and ground state are completely different. In fact, the phases multiplying the equations are chosen to accomplish this goal as well as possible. The ground state varies on the time scale of $1/(\Delta_{L1} - \Delta_L) = 2/\Delta_\omega$. In the context of recoil-induced resonances Δ_ω is usually below 100 kHz (Section 3.2). The time dependence of the excited state is dominated by the term including the detuning of the lasers, which is large compared with the natural line width of the transition Γ and usually more than a GHz. In the recoil-induced resonance experiment, those fast oscillations are of no interest and they are damped by spontaneous emissions on the time scale of $1/\Gamma$ (a few nanoseconds). It is sufficient to include this damping effect in order to take spontaneous emission into account. Neglecting them, as mentioned before, in the rest of our derivations is a good approximation. The fact that spontaneous emissions really result in a damping of the excited state motion can be understood in a density-matrix approach [9] which is beyond the scope of this thesis. The time during which the damping occurs is negligible on the overall time scale of the ground state motion because $\Delta_\omega \ll \Gamma$. Therefore, it is a good approximation to assume an instantaneous damping of the excited state motion, i.e., $\partial_t|\Psi_e\rangle = 0$ at all times. This procedure is known as adiabatic elimination of the excited state [4].

Furthermore, for atoms cooled roughly to the Doppler limit (Section 2.2.2) we can use $p^2/2m \ll \hbar\Delta_L$. This reduces the equation of motion of the

excited state to

$$|\Psi_{\mathrm{e}}\rangle = \frac{1}{\hbar\Delta_{\mathrm{L}}}\Big(\frac{\hbar\Omega_1}{2}e^{i\vec{k}_1\cdot\vec{r}} + \frac{\hbar\Omega_2}{2}e^{i\vec{k}_2\cdot\vec{r}}e^{i\Delta_\omega t}\Big)|\Psi_{\mathrm{g}}\rangle. \tag{3.20}$$

Using this explicit form of the excited state in the Schrödinger equation for the ground state results in

$$\begin{aligned} i\hbar\partial_t|\Psi_{\mathrm{g}}\rangle = \frac{p^2}{2m}|\Psi_{\mathrm{g}}\rangle + \hbar(\Delta_{\mathrm{L1}} - \Delta_{\mathrm{L}})|\Psi_{\mathrm{g}}\rangle \\ + \frac{\hbar\Omega_1}{4\Delta_{\mathrm{L}}}\Big(\Omega_1 + \Omega_2 e^{-i(\vec{k}_1-\vec{k}_2)\vec{r}}e^{i\Delta_\omega t}\Big)|\Psi_{\mathrm{g}}\rangle \\ + \frac{\hbar\Omega_2}{4\Delta_{\mathrm{L}}}\Big(\Omega_1 e^{i(\vec{k}_1-\vec{k}_2)\vec{r}}e^{-i\Delta_\omega t} + \Omega_2\Big)|\Psi_{\mathrm{g}}\rangle \end{aligned} \tag{3.21}$$

or

$$\begin{aligned} i\hbar\partial_t|\Psi_{\mathrm{g}}\rangle = \frac{p^2}{2m}|\Psi_{\mathrm{g}}\rangle + \hbar(\Delta_{\mathrm{L1}} - \Delta_{\mathrm{L}} + \omega_{\mathrm{AC}})|\Psi_{\mathrm{g}}\rangle \\ + \frac{\hbar\Omega_{\mathrm{R}}}{2}\Big(e^{-i(\vec{k}_1-\vec{k}_2)\vec{r}}e^{i\Delta_\omega t} + e^{i(\vec{k}_1-\vec{k}_2)\vec{r}}e^{-i\Delta_\omega t}\Big)|\Psi_{\mathrm{g}}\rangle, \end{aligned} \tag{3.22}$$

where we have introduced $\omega_{\mathrm{AC}} = (\Omega_1^2 + \Omega_2^2)/(4\Delta_{\mathrm{L}})$ and $\Omega_{\mathrm{R}} = \Omega_1\Omega_2/(2\Delta_{\mathrm{L}})$. Here, ω_{AC} represents the Stark shift of all motional states due to the laser light, and Ω_{R} is the effective Rabi frequency of the stimulated Raman transitions between motional states.

The second term in Equation (3.22) represents only an energy offset that is the same for all the motional states and can be set to zero (which requires another phase transformation). The second term includes factors of the form $e^{\pm i(\vec{k}_1-\vec{k}_2)\vec{r}}$ which increase or decrease the momentum of a motional state. In terms of operators $e^{\pm i(\vec{k}_1-\vec{k}_2)\vec{r}}$ acting on momentum eigenstates $|\Psi_{\vec{p}}\rangle$ labeled by their momentum eigenvalue $\vec{p}$ that means

$$\begin{aligned} e^{i(\vec{k}_1-\vec{k}_2)\vec{r}}|\Psi_{\vec{p}}\rangle = |\Psi_{\vec{p}-\ (\vec{k}_1-\vec{k}_2)}\rangle \\ e^{-i(\vec{k}_1-\vec{k}_2)\vec{r}}|\Psi_{\vec{p}}\rangle = |\Psi_{\vec{p}+\ (\vec{k}_1-\vec{k}_2)}\rangle. \end{aligned} \tag{3.23}$$

Now we have the proper tools to make the transitions between motional states explicit in our formalism. For simplicity let us assume that our atoms can only occupy two distinct motional states $|\Psi_{\vec{p}}\rangle$ and $|\Psi_{\vec{p}+\Delta\vec{p}}\rangle$, chosen to be momentum eigenstates. Therefore, the most general motional state can be written as $|\Psi_{\mathrm{g}}\rangle = \alpha|\Psi_{\vec{p}}\rangle + \beta|\Psi_{\vec{p}+\Delta\vec{p}}\rangle$. In this two level system we can explicitly express the operators $e^{\pm i(\vec{k}_1-\vec{k}_2)\vec{r}}$ by their matrix elements and the corresponding creation and annihilation operators. If $\Delta\vec{p} \neq \hbar(\vec{k}_1 - \vec{k}_2)$ all the matrix elements are zero because of the orthogonality of momentum eigenstates. The states are simply not coupled and only evolve freely. This is how momentum conservation appears in this problem. A transition is only possible if the momentum transfer by a photon matches the momentum change of the atom. If $\Delta\vec{p} = \hbar(\vec{k}_1 - \vec{k}_2)$, the non-diagonal matrix elements $\langle\Psi_{\vec{p}+\Delta\vec{p}}|e^{-i(\vec{k}_1-\vec{k}_2)\vec{r}}|\Psi_{\vec{p}}\rangle$ and $\langle\Psi_{\vec{p}}|e^{i(\vec{k}_1-\vec{k}_2)\vec{r}}|\Psi_{\vec{p}+\Delta\vec{p}}\rangle$ are unity (Equation (3.23)), and the equation of motion becomes

$$\begin{aligned} i\hbar\partial_t\Big(\alpha|\Psi_{\vec{p}}\rangle + \beta|\Psi_{\vec{p}+\Delta\vec{p}}\rangle\Big) = \alpha\frac{\vec{p}^{\,2}}{2m}|\Psi_{\vec{p}}\rangle + \beta\frac{(\vec{p}+\Delta\vec{p})^2}{2m}|\Psi_{\vec{p}+\Delta\vec{p}}\rangle \\ + \frac{\Omega_{\mathrm{R}}}{2}\Big(\beta e^{-i\Delta_\omega t}|\Psi_{\vec{p}}\rangle + \alpha e^{i\Delta_\omega t}|\Psi_{\vec{p}+\Delta\vec{p}}\rangle\Big). \end{aligned} \tag{3.24}$$

Formally, this equation of motion is equivalent to that of a pure two-level system with an energy separation of $((\vec{p}+\Delta\vec{p})^2 - \vec{p}^{\,2})/(2m) > 0$ for $\Delta_\omega < 0$ or $((\vec{p}+\Delta\vec{p})^2 - \vec{p}^{\,2})/(2m) < 0$ for $\Delta_\omega > 0$. Otherwise, the terms in the Hamiltonian correspond to those dropped usually in the rotating wave approximation and the coupling between the states is negligible. The transitions are driven with a Rabi frequency Ω_{R}, as defined above, by a light field with frequency Δ_ω. So, we have finally reduced the problem of investigating stimulated Raman transitions between motional states to the well-known problem

of a two-level system. We can use the effective Hamiltonian

$$\begin{aligned} H =& \frac{\vec{p}^2}{2m}|\Psi_{\vec{p}}\rangle\langle\Psi_{\vec{p}}| + \frac{(\vec{p}+\Delta\vec{p})^2}{2m}|\Psi_{\vec{p}+\Delta\vec{p}}\rangle\langle\Psi_{\vec{p}+\Delta\vec{p}}| \\ &+ \frac{\Omega_{\mathrm{R}}}{2}e^{-i\Delta_\omega t}|\Psi_{\vec{p}}\rangle\langle\Psi_{\vec{p}+\Delta\vec{p}}| + \frac{\Omega_{\mathrm{R}}}{2}e^{i\Delta_\omega t}|\Psi_{\vec{p}+\Delta\vec{p}}\rangle\langle\Psi_{\vec{p}}| \end{aligned} \tag{3.25}$$

to make predictions for recoil-induced resonances.

Naturally, taking only two motional states into account is not realistic. However, momentum conservation, as we have seen before, ensures that each state can be coupled to only two others. Therefore, the error is small when we consider one motional state and one of the states coupled to it at a time and add up the results. This is in particular true since, under typical operating conditions, the momentum distribution is not changed substantially by the measurement, such that the possible transitions from each motional level to the two other motional states do not affect each other substantially. This fact is used again in Section 3.2 where we use first-order time-dependent perturbation theory to attack the two-level problem. It is only when other resonant effects come into play that are not covered in our simple approach or when the interaction is strong enough to invalidate our two-level approximation that our predictions become useless (Section 3.3).

3.2 Predictions for Recoil-Induced Resonances

At the beginning of this section we give a qualitative explanation for the origin of recoil-induced resonances and return to our quantitative analysis at the end. We make predictions for the lineshape of the resonance for our simple model including only two internal atomic levels. In this context we show that the recoil-induced resonances can give access to the temperature of an atomic cloud

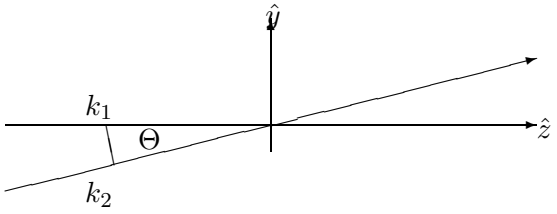

Figure 3.1: The geometry of the experiment: The two laser beams subtend a small angle Θ. To first order in Θ the difference of the wavevectors is a vector along the y-axis.

or even to its complete momentum distribution. Additionally, the investigation of our theoretical predictions in this section highlights the requirements for our experimental setup.

In Section 3.1 we have considered stimulated Raman transitions between motional states in a general case. In order to see in what way those transitions lead to a resonant structure, let us take a closer look at the laser field we use and the motional states that are actually coupled.

So far, we had to assume that the relative detuning of the two laser beams is small compared to the natural decay rate of the excited state and that they are far-detuned when we adiabatically eliminated the excited state. Now, let us be specific about the geometry of the experiment. Without loss of generality we can take $\vec{k}_1$ to be parallel to the z-axis in some coordinate system. The second beam, characterized by $\vec{k}_2$, is propagating in the yz-plane at a small relative angle Θ (Fig. 3.1). Because the relative detuning of the two laser beams is negligible compared to the optical frequency of the lasers, the magnitudes of the wave vectors are approximately equal. Therefore, we can set

$|\vec{k}_1| = |\vec{k}_2| = k$ in the following calculations. Furthermore, Θ is assumed to be small enough such that all terms of order Θ^2 are negligible. Choosing a small intersection angle for the two laser beams simplifies the following analysis. The momentum difference between the motional states coupled by the stimulated Raman transitions results in

$$\Delta\vec{p} = \hbar(\vec{k}_1 - \vec{k}_2) = \hbar k(\hat{y}\sin\Theta + \hat{z}(\cos\Theta - 1)) \approx \hbar k\Theta\hat{y}. \tag{3.26}$$

The corresponding energy difference is

$$\Delta E = \frac{(\vec{p} + \Delta\vec{p})^2}{2m} - \frac{\vec{p}^{\,2}}{2m} = \frac{2\vec{p}\Delta\vec{p} + \Delta\vec{p}^{\,2}}{2m} \approx \frac{p_y\hbar k\Theta}{m}. \tag{3.27}$$

This difference can be written as a resonant frequency ω_{res} for the transitions between the two motional states

$$\omega_{\mathrm{res}} \approx \frac{p_y k\Theta}{m}. \tag{3.28}$$

All states connected by the transition are stable ground states and therefore the width of the transition is extremely small compared with transitions involving an internal excited state of an atom. Only relaxation processes such as collisions or spontaneous emission limit the otherwise infinite lifetime of the motional state and lead to a small but non-zero width denoted in the following by γ. Therefore, in a qualitative discussion only the resonantly coupled states are of importance. This leads to another condition for the states that are actually coupled, namely

$$p_y = \frac{\Delta_\omega m}{k\Theta}, \tag{3.29}$$

where Δ_ω is the relative detuning of the lasers and, according to Section 3.1, the effective driving frequency for the transitions. At any given time only motional states with a given momentum in the y-direction close to p_y are affected by the stimulated Raman process. This means that this geometry is only sensitive to the y-direction of the momentum. Our measurement cannot distinguish motional states with different overall momenta but equal y-components. Because p_y can range, in principle, from $-\infty$ to $+\infty$, there are motional states coupled resonantly by the Raman transitions for any Δ_ω .

Raman transitions naturally have the same average transition rates between two states in either direction. Nevertheless, the overall transition rate from each state into the other in an atomic cloud is proportional to the number of atoms occupying this particular state. Each of those transitions scatters one photon from one of the beams into the other. The measurable quantity is the power variation in one of the beams, i.e., the net photon scattering rate between the two beams due to the Raman transitions. According to all these considerations this scattering rate has to be proportional to the difference in occupation number of the states coupled at each time. Therefore, an atomic cloud with equally distributed momenta would not yield a signal at all because an equal number of photons is scattered into and out of each beam. Fortunately, momenta are not equally distributed, but they are distributed according to the Maxwell-Boltzmann statistics. In thermal equilibrium there are more atoms in states with lower energy, i.e., smaller momentum. In other words, the Raman transitions will dominantly occur from lower energy states with less momentum to higher energy states with larger momentum. Therefore, the lower frequency beam always gains intensity and the higher frequency

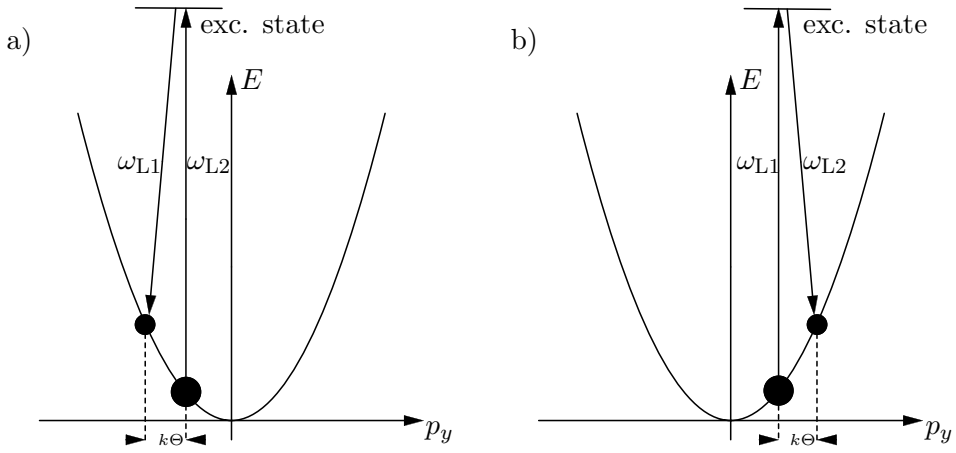

Figure 3.2: Schematic of recoil-induced resonances. The smaller the momentum the bigger is the population of a velocity class. For given laser frequencies only atoms with certain momenta can scatter photons because they fulfill energy and momentum conservation. The arrows show the net scattering of photons due to the Raman transition. In case a), $\omega_{L1} < \omega_{L2}$ and laser 1 gains intensity; for case b), $\omega_{L1} > \omega_{L2}$ and laser 1 loses intensity.

beam always loses intensity for the same reason. This process is visualized in Fig. 3.2.

At this point we can understand the origin of the recoil-induced resonances. In our experiment it is easiest to sweep the frequency of one laser linearly relative to the frequency of the other. Therefore, Δ_ω varies linearly with time, and different motional states are coupled resonantly by the Raman transitions. The momentum in y-direction of the coupled states differs only by much less than one recoil momentum (Equation (3.26)). For momentum distributions having a width larger than a single recoil, the signal at each instant of time is approximately proportional to the derivative of the distribution at

a point p_y given by Equation (3.29). Therefore, the signal during the sweep through zero detuning is approximately proportional to the derivative function of the momentum distribution around zero momentum (see below for a mathematical derivation). Clearly, the linearity of the sweep is important for the analysis of the resonance. Instabilities in the relative frequency lead to distortions of the obtained signal.

At temperatures where the width of the momentum distribution is too large to be comparable to the recoil momentum, one cannot expect to see a signal because this derivative is negligibly small. However, an atomic cloud cooled down beyond the Doppler limit (Section 2.2.2) shows variations in the momentum distribution that are large enough to yield a signal. This is the reason that recoil-induced resonances have only been observed in cold-atom physics so far.

Now that we have shown a qualitative picture of the origin for recoil-induced resonances, it is time to come back to our quantitative calculations. Having reduced the problem of stimulated Raman transitions to a two-level system one can use the textbook results for these systems. The recoil-induced resonance measurement is done in a fast sweep of Δ_ω such that each motional state is in resonance for a transition only for a short time interval. In fact, the sweep should be fast enough not to significantly disturb the momentum distribution, which is being measured. Moreover, a long sweep would lead to many spontaneous emission events and therefore heat the atoms. Thus, we chose the experimental parameters such that we can hope that a perturbative solution for the transition rate from one motional state into another is suffi-

cient. Taking into account the width of the transition this transition rate W for a two-level system is generally given by [10]

$$W = \Omega^2 \frac{\frac{\Gamma}{2}}{\Delta^2 + \frac{\Gamma}{2}^2}, \tag{3.30}$$

where Ω is the Rabi frequency of the problem, Δ is the detuning of the driving field from resonance, Γ is the decay rate of the excited state and the usual limitations of time-dependent perturbation theory apply.

In analogy, in the special case of a two-level system of motional states coupled by stimulated Raman transitions as described by the Hamiltonian in Equation (3.25) the result presented in Equation (3.30) reads

$$W = \omega_{\mathrm{R}}^2 \frac{\gamma}{(\Delta_\omega - \frac{p_y k \Theta}{m})^2 + \gamma^2}, \tag{3.31}$$

where the detuning is explicitly expressed through the driving frequency and the momentum in y-direction of one of the coupled states. Here, γ is the relaxation parameter for the motional states as introduced before and is equivalent to the inverse lifetime in electronic transitions.

As described before, the transition rate is equal for the Raman process in both directions. The direction of the scattering of a photon from one beam into the other depends only on the initial state of the scattering atom. Therefore, in mathematical terms, the overall photon scattering rate δ_{ph} measured (instantaneously) in the experiment is

$$\delta_{\mathrm{ph}} = \Omega_{\mathrm{R}}^2 \int_{p_y} dp_y \frac{\gamma\Big(\Pi(p_y) - \Pi(p_y + \hbar k \Theta)\Big)}{(\Delta_\omega - \frac{p_y k \Theta}{m})^2 + \gamma^2}, \tag{3.32}$$

where $\Pi(p_y)$ and $\Pi(p_y + \hbar k \Theta)$ denote the population densities of the motional states with a given momentum in y-direction. The integral arises because, in

principle, we have to take into account all the motional states in the atomic cloud, although almost all of them are far from resonance.

This scattering rate results in an intensity change in both beams as a function of Δ_ω. Let us try to make a quantitative prediction for the lineshape for atoms with a momentum distribution corresponding to Maxwell-Boltzmann statistics in a recoil-induced resonance experiment. To accomplish this goal we must make several more approximations. We assume a momentum distribution with a width of a few $\hbar k$. The difference in momentum between two coupled states is $\hbar k\Theta$. Because Θ is small, the two coupled states are close together compared to the scale of the whole distribution. Furthermore, we can expect the momentum distribution to vary smoothly and therefore approximate

$$\Pi(p_y) - \Pi(p_y + \hbar k\Theta) \approx -\hbar k\Theta \partial_{p_y}\Pi(p_y). \tag{3.33}$$

Additionally, we can use the identity

$$\lim_{\gamma\to 0} \frac{\gamma}{(\Delta_\omega - \frac{p_y k\Theta}{m})^2 + \gamma^2} = \delta(\Delta_\omega - \frac{p_y k\Theta}{m}), \tag{3.34}$$

because γ is small for motional states. Altogether we find

$$\delta_{\mathrm{ph}} \propto \Omega_{\mathrm{R}}^2 \hbar k\Theta \partial_{p_y}\Pi(p_y)\big|_{p_y=\frac{\Delta_\omega m}{k\Theta}}. \tag{3.35}$$

Plugging in an atomic distribution $\Pi(p_y)$ according to the Maxwell-Boltzmann statistics

$$\Pi(p_y) = N\frac{1}{\sqrt{\pi 2mk_{\mathrm{B}}T}} e^{\frac{-p_y^2}{2mk_{\mathrm{B}}T}}, \tag{3.36}$$

where N is the total number of atoms, we have a scattering rate, or equivalently

a variation in measured power ΔP as a function of Δ_ω given by

$$\begin{aligned}\Delta P &\propto -N\frac{k\Theta\Omega_{\mathrm{R}}^2}{\sqrt{k_{\mathrm{B}}T}}\frac{\Delta_\omega}{(k\Theta)k_{\mathrm{B}}T}\exp\frac{-m\Delta_\omega^2}{2(k\Theta)^2k_{\mathrm{B}}T}\\ &\propto -N\frac{\Omega_1^2\Omega_2^2}{4\Delta_{\mathrm{L}}^2}\frac{\Delta_\omega}{(k_{\mathrm{B}}T)^{\frac{3}{2}}}\exp\frac{-m\Delta_\omega^2}{2(k\Theta)^2k_{\mathrm{B}}T}.\end{aligned} \tag{3.37}$$

Therefore, a plot of one laser's power after the interaction with the atoms versus relative detuning between the two beams should look like a derivative of a Gaussian on top of an offset due to the power in the beam when no resonant interaction occurs. Because only a small fraction of the atoms is interacting at any time and we want to perturb the system as little as possible, we have to expect only a small variation in the overall measured power. All quantities except the temperature are directly measurable in the experimental setup. This shows that the recoil-induced resonance can, in principle, give direct access to the temperature of an atomic cloud. The higher the temperature, the broader and less pronounced is the resonance.

Furthermore, we see that the signal scales with the inverse square of the laser detuning and linearly with both of the laser intensities. A smaller angle reduces the width of the signal in addition to the amplitude. The reduction of the amplitude can be seen by explicitly computing the amplitude at the extrema of the Gaussian derivative. This result of our calculations does not agree with the result in [2] that predicts an amplitude independent of the angle.

Compared with other spectroscopic resonances, the recoil-induced resonance is extremely narrow. An atomic cloud with a typical temperature in cold-atom physics corresponding to a momentum distribution with a width of

$10\hbar k$ yields a resonance structure (according to Equation (3.28)) with 82 kHz $\times\Theta$ difference between the two peaks of the derivative.

Note at this point that this theoretical analysis does not restrict the measurement process of recoil-induced resonances to thermal distributions. In general, a given momentum distribution will always yield a signal proportional to its first derivative with respect to momentum. Therefore, recoil-induced resonances could be used as a general method for spectroscopic velocimetry of cold atoms.

3.3 Beyond The Ideal Theory

In this section we explore the limits of the theoretical approach given in Sections 3.1 and 3.2 and try to investigate which features of a real system can alter our simple model significantly. Naturally, this effort has to be phenomenological. We start with the effects of a more realistic laser field (Section 3.3.1) and then describe the effects of the complicated electronic level structure in real atoms (Section 3.3.2). Finally, the dynamic nature of the experiment is compared with our theoretical assumptions (Section 3.3.3).

3.3.1 The Laser Fields

In Equation (3.2) we assumed a laser field consisting of two different plane waves. Of course, this model is an idealization because in our experiment, laser beams are used that have a beam width comparable to the dimensions of the atomic cloud. This means that the strength of the electric field varies considerably across the atomic cloud, and the coupling strength of the Raman

process differs from atom to atom.

As long as the momentum distribution is approximately homogeneous in space this effect should not alter the overall result. Only if the homogeneity is greatly disturbed would the predicted line shape be altered. For example, if the fast atoms were predominantly located on the periphery of the atomic cloud and the slow ones at the center, the signal from the faster ones would be suppressed because the weaker light field would lead to less scattered light.

Furthermore, in our experimental setup, the laser beams are focused on the atoms. Therefore, the perfect directionality of the light expressed in the two wave vectors $\vec{k}_1$ and $\vec{k}_1$ is not realistic. Nevertheless, the variation of those wave vectors across the atomic cloud is extremely small, so that this effect should lead only to negligible variations in the predictions for our line shape.

Additional light from other sources that can disturb the free atomic motion can also disturb the recoil-induced resonances in an unpredictable way. Unfortunately, we have to include such an additional light source, the so-called repump laser because of the structure of the used cesium transition (Sections 3.3.2 and 4.2). However, it is far-detuned compared with all other light sources and we can hope that its effect is negligible.

3.3.2 Multiple States

Another simplification in our theoretical approach to Raman transitions in Section 3.1 is that we considered an internal electronic structure of the atoms consisting of only two levels. The internal structure of the cesium D_2 transition

used in our experiment is far more complicated. The hyperfine structure of the $6^2S_{1/2}$ and $6^2P_{3/2}$ states coupled by this transition is shown in Appendix A.

The Raman transitions are driven between motional levels of the $6^2S_{1/2}$ $F = 4$ state of cesium. The lasers only couple the $F = 4$ states to the excited state via the Raman transitions because the detuning for transitions involving the $F = 3$ states is much larger. (Remember that the predicted signal scales with the inverse of the detuning squared.) Only when many spontaneous emissions occur due to the two lasers can the $F = 3$ state become important because atoms can end up in the $F = 3$ state after a spontaneous emission cycle. To transfer these atoms back to the $F = 4$ state the repump laser is included in the setup (Section 4.2).

Even more complicated is the structure of the $6^2P_{3/2}$ excited states of the cesium D_2 line. Because the hyperfine splitting of this level is much smaller, all hyperfine sublevels are almost equally far detuned (Appendix A), and the Raman process can be driven through each of them. Therefore, in principle, the assumption of only one excited state in Section 3.1 has to be modified. Instead of one coupling term of the form

$$\frac{\hbar\Omega_1}{2}\left(ae^{-i\vec{k}_1\cdot\vec{r}}e^{i\omega_{\mathrm{L}1}t} + a^\dagger e^{i\vec{k}_1\cdot\vec{r}}e^{-i\omega_{\mathrm{L}1}t}\right) \tag{3.38}$$

in the interaction Hamiltonian (Equation (3.11)) we have to consider a whole sum of terms

$$\sum_i \frac{\hbar\Omega_{i1}}{2}\left(a_i e^{-i\vec{k}_1\cdot\vec{r}}e^{i\omega_{\mathrm{L}1}t} + a_i^\dagger e^{i\vec{k}_1\cdot\vec{r}}e^{-i\omega_{\mathrm{L}1}t}\right), \tag{3.39}$$

where i runs over all sublevels within the hyperfine structure, which are coupled to a given ground state. It turns out that this is not a real complication because it only results in a change of the effective Rabi frequency for the Raman transition. Including the structure of the excited state it is given by

$$\Omega_{\mathrm{R}} = \sum_i \frac{\hbar \Omega_{i1} \Omega_{i2}}{2\Delta_{\mathrm{L}i}}. \tag{3.40}$$

Additionally, the ground state $6^2S_{1/2}$ $F = 4$ consists of no less than 9 magnetic sublevels. If the lasers are linearly polarized in the same direction, only $\Delta m = 0$ transitions occur and the multi-level structure should not be important. Only another sum over the ground states should enter the calculation, in analogy to our considerations of the excited states. However, including these sublevels in the calculation for other polarizations turns out to be an involved process and is no longer possible in our simple approach. As a result, intensive density-matrix calculations show that degenerate levels can lead to other resonant structures due to Raman transitions between different levels [11]. These resonances can be as narrow as the recoil-induced resonances and add to the the signal derived in Section 3.2. In certain polarization configurations those additional resonances can spoil the usefulness of recoil-induced resonances for velocimetry of cold atoms, because the information about the momentum distribution is hidden behind other effects.

3.3.3 Dynamics

Another problem of the simple theoretical approach presented in this chapter is that it does not account for all the dynamics in the real experiment. First of all the sweep is not included directly in the derivation of our signal. It is only used

as a justification of our perturbative approach. Equation (3.31) is only valid in the perturbative limit for times after the perturbing interaction is applied much longer than the decay rate of the excited state. In an experiment where the resonantly coupled states are changing with time this limit is questionable and has to be tested in the experiment. Furthermore, the intensity limit where the perturbative approach breaks down because the interaction becomes too strong is not known.Therefore, we cannot be sure that our experimental parameters allow for a perturbative treatment.

Also, the dynamical movement of the atoms in the position-dependent laser field during the interaction time is not accounted for. The atoms are moving in a standing wave in the direction of momentum transfer. This makes the effective Rabi frequency also position-dependent. This dependence is ignored in our calculation as are the variations in the laser field over the atomic cloud due to the small beamwidth (Section 3.3.1).

Chapter 4

Cold Atoms in the Experiment

In this chapter we discuss how the different requirements for a cesium MOT are satisfied in the experiment. As described in Section 2.2, only certain atoms (those with closed cycling transitions) can be cooled and trapped in a MOT. As we will see during the discussion of the MOT beams in Section 4.2, cesium can, in principle, provide such a transition. However, we first describe the vacuum chamber (Section 4.1) that is used in our experiment. We finish the chapter with a description of the magnetic field (Section 4.3).

4.1 Vacuum Chamber

A MOT is extremely sensitive to the background pressure because collisions with thermal untrapped atoms limit the efficiency of this trapping method. In order to reduce these collisions it is necessary to enclose the cesium atoms in a vacuum chamber and to make sure that the cesium pressure itself is not too high.

In our experiment we use an ultra-high vacuum (UHV) chamber with a pressure of about 8×10^{-8} torr to enclose the cesium atoms. The vacuum is sustained by a Varian ion pump (model 919-0236) after the UHV has been

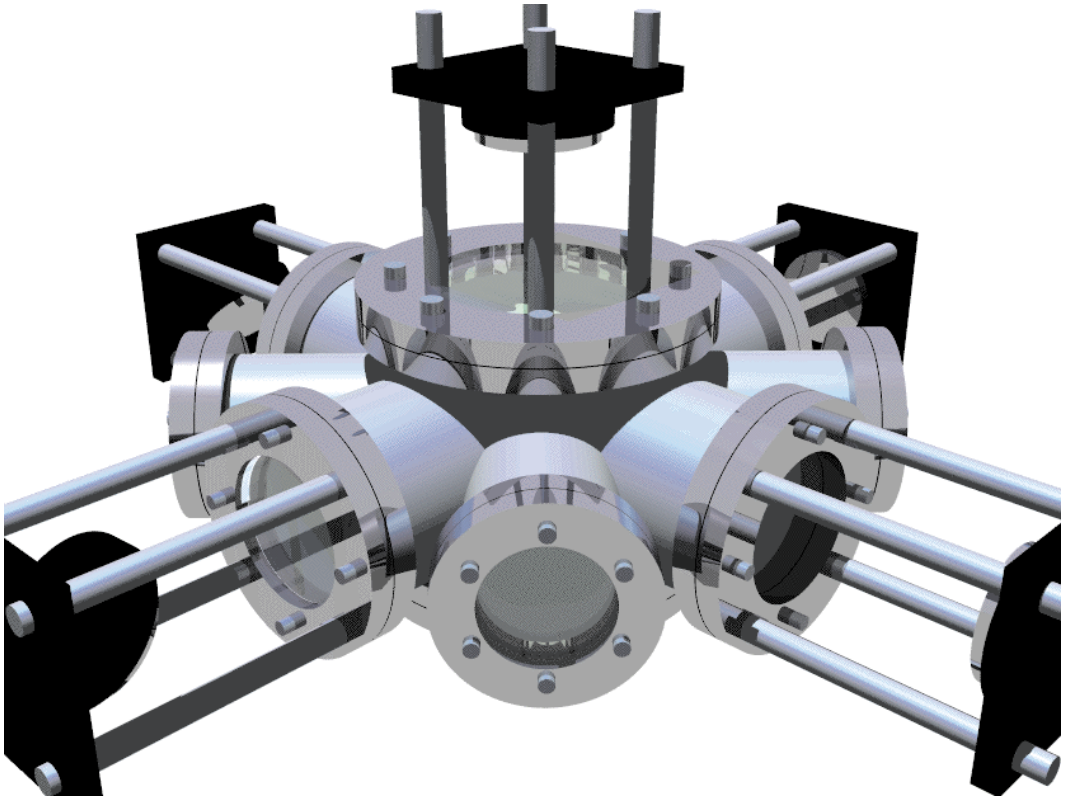

Figure 4.1: Sketch of the vacuum chamber. A computer generated picture shows the vacuum chamber with its windows. The mirrors for guiding the beams through the chamber and reflecting them back are also shown including their mounts. The quarter-wave plates are omitted for clarity. (Graphics by Windell H. Oskay)

created by a turbo pump.

The chamber has ten anti-reflection coated windows to allow different beams to enter the chamber. The six 2.5 inch diameter windows define the x, y, and z axes while the four smaller 1.25 inch diameter windows form a cross in the horizontal plane at 45° relative to the $x - y$ axes (see Fig. 4.1). The six large windows are used for the MOT beams (Section 4.2). One of the smaller ports gives access to the CCD camera, which is used for time-of-

flight (TOF) measurements, while the opposite window is covered, supplying a dark background for the camera pictures. This port also provides access to the chamber for the cesium source and the ion pump. The other two small windows are not used for the recoil-induced resonance experiments described in this thesis.

The cesium is stored in a glass ampoule that is connected to the chamber through two UHV valves (Varian model 951-5027). The inner valve is left wide open and might only be used to remove the cesium ampule without breaking vacuum. The outer valve is normally lightly closed. Because the ion pump constantly removes cesium atoms from the chamber it must be opened one or two turns on a time scale of once per week. Then, the vapor pressure of the cesium (2×10^{-5} torr at room temperature) is sufficient to repopulate the chamber with cesium. It is important to close the valve again after about 15 minutes, because otherwise the chamber becomes flooded and the pressure is too high for reasonable experiments.

4.2 The MOT Beams

In order to trap and cool atoms in our vacuum chamber, we need three pairs of counterpropagating beams (see Sections 2.2 and 2.4). Additionally, one needs a so-called repump beam because of the special properties of the cesium transition used for trapping.

The theoretical description of the Doppler cooling in Section 2.2 is idealized in the sense that an atom is described as a two-level system. By contrast, the cesium D_2 line, which is important for our experiments has, a

rather complicated electronic structure shown in Appendix A. The ($6\,^2S_{1/2}$, $F = 4$) to ($6\,^2P_{3/2}$, $F' = 5$) transition is used for Doppler cooling, i.e., the cooling and trapping beams are much further detuned with respect to the ($F = 4 \rightarrow F' = 4$) and ($F = 4 \rightarrow F' = 3$) than is needed for effective Doppler cooling. The ($F = 4 \rightarrow F' = 5$) transition is used because the selection rule $\Delta F = 0, \pm 1$ ensures that all the excited states that decay via dipole transitions return to the $F = 4$ state. However, the hyperfine splitting of the $6\,^2P_{3/2}$ excited state is not large. Therefore, the detuning from the ($F = 4 \rightarrow F' = 4$) and ($F = 4 \rightarrow F' = 3$) is not large enough to completely suppress spontaneous emission cycles with excited states $F' = 3$ and $F' = 4$. Unfortunately, these excited states can decay to the ($6\,^2S_{1/2}$, $F = 3$) state, which does not interact with the MOT beams because the detuning is large (9 GHz). This state is therefore often referred to as a dark state. After a short time one would thus end up with all atoms in the ($6\,^2S_{1/2}$, $F = 3$) state and lose the possibility of further cooling. To circumvent this effect one uses a second laser that drives the transitions from the $F = 3$ state to the $6\,^2P_{3/2}$ levels. Part of these pumped atoms return into the desired $F = 4$ level. In other words, the laser pumps atoms back into the level that is used for cooling, and it is therefore called the repump laser.

Section 4.2.1 introduces the laser and the optical setup for the trapping and cooling beams. In Section 4.2.2 we discuss the repump laser and its implementation in the experiment.

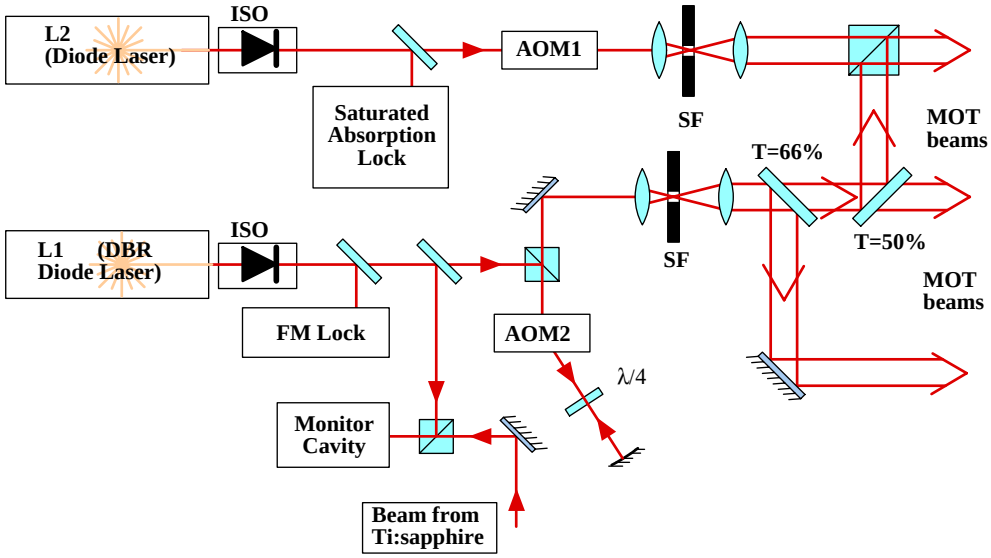

Figure 4.2: Optical setup for the MOT beams. The FM lock and the saturation absorption lock are only shown symbolically. Their own optical setup is rather complicated [12]. The monitor cavity and the Ti:sapphire laser are not related to cooling and trapping and are explained in Chapter 5. (Graphics by Windell H. Oskay)

4.2.1 Trapping Beams

The laser providing the cooling and trapping beams for the MOT is an SDL-5812-H1 Distributed Bragg Reflector (DBR) laser diode (L1 in Fig. 4.2). It is operated at a temperature of 15 °C, controlled by an internal thermoelectric cooler.

After shaping the beam with an anamorphic prism pair, sending it through an optical isolator, splitting 10% off for the FM lock and spatially filtering it, one gets about 8.5 mW/cm^2 maximum intensity in a beam with waist 11 mm. The FM lock stabilizes the frequency of the laser via a feedback loop based on saturated absorption FM spectroscopy (see [12,13] for details).

The laser is locked to the crossover line between ($F = 4 \rightarrow F' = 4$) and ($F = 4 \rightarrow F' = 5$) of the hyperfine spectrum. Due to this FM lock the output frequency of the DBR laser is detuned 195 MHz to the red of the ($F = 4 \rightarrow F' = 5$) transition. This offset is compensated by AOM2 (see Fig. 4.2), which has a frequency modulation input and shifts the frequency by between +120 MHz and +200 MHz. The frequency of the trapping beams is therefore tunable between -75 MHz and +5 MHz from the $F = 4 \rightarrow F' = 5$ transition (Appendix A). We usually operate at -15 MHz detuning. The AOMs additionally provide a simple method for controlling the beam intensity. The variation of detuning and intensity during the recoil-induced resonance experiment is shown in Section 5.3.

The appropriately modulated beam is split into three beams with equal intensities, which are directed through the chamber in x, y and z direction. They are retroreflected at each opposite port such that there are two counterpropagating beams in all three spatial directions, as is needed for Doppler cooling. To allow trapping, the beams need to be $\sigma^+ - \sigma^-$ polarized. Therefore, a quarter-wave plate is included in front of the chamber to change the polarization from linear to circular. Note that the optical axis of the the quarter-wave plate has to be aligned at 45° with respect to the beams' polarization to affect the polarization in this way. A second quarter-wave plate after the chamber changes the polarization from σ^+ to σ^- or vice versa because the beam passes twice through the quarter-wave plate.

4.2.2 Repump Beam

In our setup the repump beam is supplied by a Littrow-configuration grating-stabilized diode laser system (L2 in Fig. 4.2). The diode itself is an SDL-5421-G1 model that produces about 40 mW of single-mode light with a driving current of 93 mA.

The frequency of the repump is stabilized with a saturated absorption lock. It is locked to the $(F = 3 \rightarrow F' = 3, 4)$ crossover transition. A 100 MHz AOM (AOM1 in Fig. 4.2) shifts the light by 100 MHz onto the $F = 3 \rightarrow F' = 4$ transition. This AOM also acts as a fast shutter for the light.

Filtering and expanding the beam in a similar fashion as the trapping beam provides about 16 mW in a beam with 1 cm waist. It is combined with the vertical trapping beam through a polarizing beamsplitter that takes advantage of the fact that the two lasers' polarizations are at 90° (see top right of Fig. 4.2). The beams are then directed through the chamber in vertical direction. For a more detailed description of the repump laser and the locking method see Klappauf [12].

4.3 Realization of the Magnetic Field

A three-dimensional magnetic field gradient, which is necessary for trapping (Section 2.3), can be realized with a pair of coils in the anti-Helmholtz configuration. The coils are placed at a distance $d = R$ where R is the radius of each coil. In our setup the two coils are mounted symmetrically about the center of the vacuum chamber in horizontal planes (so that the z-axis is a symmetry axis). Contrary to the Helmholtz configuration, the currents in the two coils

run in opposite directions.

Due to the cylindrical symmetry of this configuration, the gradients of the magnetic field $\vec{B}$ are equal in the x and y directions, i.e.,

$$\frac{\partial B_x}{\partial x} = \frac{\partial B_y}{\partial y} \tag{4.1}$$

on the z axis. From Maxwell's equations we know that $\vec{\nabla} \cdot \vec{B} = 0$. Therefore, we get the relation

$$\frac{\partial B_z}{\partial z} = -2\frac{\partial B_x}{\partial x} = -2\frac{\partial B_y}{\partial y} \tag{4.2}$$

between the different components of $\vec{B}$ close to the origin. Expanding the partial derivatives of the magnetic field around the origin and taking into account that $\vec{B} = 0$ at the origin in an anti-Helmholtz configuration, this results in $B_z = cz$, $B_x = (-c/2)x$ and $B_y = (-c/2)y$ in the lowest order approximation, where c is some constant depending on the coils used. This configuration therefore provides the desired magnetic field gradient in all three dimensions.

The coils in our experiment have a radius of about 3.1 inches with 202 turns of 0.020" diameter copper magnet wire. The current of about 3 A in each coil is driven by two pairs of LM12, 36 volt, high-power opamps (one pair for each coil). This current results in a field gradient of 11 G/cm along the z axis and half of this value perpendicular to the axis. Each coil has a resistance of about 8.7 Ω, which leads to 80 W of power dissipated in each coil. Thus, the coils need to be water cooled. For a more detailed description, the reader is referred to [12].

Chapter 5

Experiments on Recoil-Induced Resonances

In Chapter 4 we introduced our general setup for producing cold atoms. Now, we can discuss how all the other requirements on the experiment found in the theoretical analysis are satisfied in our setup. The setup can be divided into several different parts, which are separately discussed in the following sections. We begin with the optical setup in Section 5.1, continue with the electronics necessary to take data and to control the frequencies of the recoil-induced resonance beams in Section 5.2, discuss the data acquisition in Section 5.3, and finally describe the analysis of the obtained resonances in Section 5.4. The analysis is shown at the example of a measured lineshape that is as similar to the theoretical predictions as possible. The same analysis with other lineshapes measured in our experiments can lead to meaningless results (Chapter 6).

5.1 Optical Setup and Alignment

Naturally, the optical setup is the heart of any spectroscopic experiment. There are three important requirements on our optical setup that make measurements of recoil-induced resonances possible. First, we need to control the

relative detuning of two laser beams to within a few hundred Hz while sweeping the frequency of one beam up to several hundred kHz around the other beam's frequency. Second, as we will see in Section 5.3, a short, well-defined interaction time between the atoms and the laser light is required. Therefore, the capability of switching the light on and off quickly is important. Third, the recoil-induced resonance itself has to be measured. This measurement is not trivial because we expect a small signal on top of a large background (see also Section 5.2.2).

5.1.1 Setup

The optical setup is shown in Fig. 5.1. The light used in our experiment is produced by a Ti:sapphire laser (see [12] for details). This laser is pumped by an argon-ion laser (Coherent Innova 90) that usually puts out (8.0 ± 0.2) W. The Ti:sapphire laser is home-built and converts this input light into a single-mode (spatially and longitudinally) beam containing up to 600 mW.

Although the Ti:sapphire laser can operate for hours without large power fluctuations, it usually has to be adjusted on a timescale of 30 minutes in order to maintain a stable output. The short timescale noise (above 10 kHz) in the light power varies between 2% and 5% depending on the overall performance of the laser. The noise is a real problem because the interesting signal is below 1% of the power. Therefore, our detection method must be able to filter out these large fluctuations (Section 5.2).

Besides stable power, the frequency of the emitted light is extremely important for the success of our experiment. The linewidth of the laser is

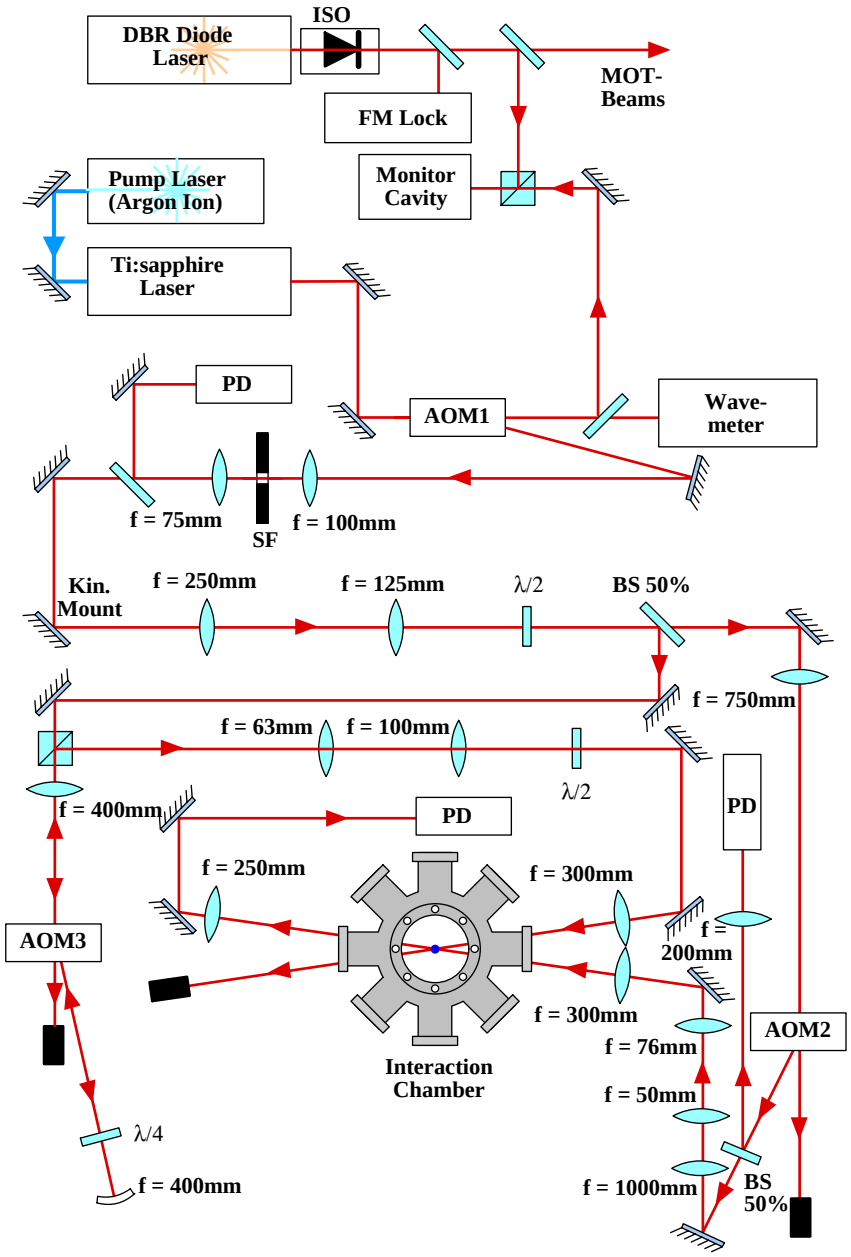

Figure 5.1: The experimental setup. PD denotes photodiodes, SF spatial filters, ISO optical isolators, and AOM acousto-optic modulators. See text for details.

10 MHz, and we need to detune it between 500 MHz and 6 GHz from resonance with a stability of better than 100 MHz in order to investigate recoil-induced resonances for different detunings. The Ti:sapphire laser is not actively locked to a certain frequency like the diode lasers in the experiment (Section 4.2). Nevertheless, the frequency is tunable [12] in the desired range and stable on the timescale of our experiment (1 ms). However, spontaneous mode hopping occurs from time to time and requires resetting of the frequency.

The coarse frequency is measured with a wavemeter (NIST Lambda Meter LM 11) by comparing it with a stabilized He:Ne laser. The fine tuning can be accomplished by monitoring the frequency of the Ti:sapphire laser and the locked DBR diode with the same Fabry-Perot cavity and using this reading to tune it to the desired frequency. Therefore, detunings are always stated with respect to the DBR laser frequency (Section 4.2).

The geometry of the setup for this frequency control is shown in the top third of Fig. 5.1. A beam splitter deflects part of the Ti:sapphire beam into the monitor cavity. The DBR laser light is coupled into the cavity by a polarizing beamsplitter, which uses the fact that the polarizations of the DBR and the Ti:sapphire laser are perpendicular. The DBR laser itself is explained in more detail in Section 4.2.

The central role in satisfying the requirements for the setup as introduced before is played by Acousto-Optic Modulators (AOM's). The basic mechanism underlying these modulators and the important parameters in operating them are described in detail in Appendix B. The acousto-optic modulator, denoted by AOM1 in Fig. 5.1, operates as a switch to direct the light

either into the wavemeter or through the rest of the recoil-induced resonance setup. An IntraAction 80 MHz AOM is used for this purpose. The 80 MHz shift up of the light frequency in the first diffraction order (used in our setup) of the AOM is of no overall importance, but it must be taken into account when the detuning is chosen. The diffraction efficiency in this order is up to 80-85%. Using the first diffraction order makes sure that no light enters the vacuum chamber when the AOM is turned off. Therefore, no light disturbs the atoms before or after the actual measurement. The rise time of the AOM, i.e., the time it needs to "switch" the light from zero to full intensity is 70 ns and therefore extremely short on the timescale of our experiment. Furthermore, within a certain range (see below for restrictions), the AOM is used to control the overall intensity in the beams used for the recoil-induced resonance experiments. Our theoretical analysis makes no predictions about the overall power level that is suitable in recoil-induced resonance experiments. Therefore, the power (like the detuning) is a free parameter that should be tunable in order to investigate the resonances. Details on the switching process and the intensity control are discussed in Section 5.3 together with the electronics driving the AOM.

In the case that the AOM is running, the diffracted light for the recoil-induced resonance experiment propagates through a spatial filter, denoted as SF in Fig. 5.1. In other words, it is focused down tightly with a 100 mm focal length lens, and a 50 μm pinhole is placed at the focal spot. Only the TEM_{00} mode [14] can pass through this pinhole, and the outgoing beam has a nice approximately Gaussian profile. After the pinhole, the beam is again collimated with a second 75 mm spherical lens. Therefore, the beam is slightly

smaller after the spatial filter because of the lenses' different focal lengths.

A beamsplitter is inserted in the beam path to deflect approximately 1% of the light towards a standard photodiode used for triggering purposes as described in Section 5.3.

The setup described so far is identical to the setup of other experiments in our group that use the same Ti:sapphire laser beam. In order to use the same laser for different purposes without major changes in the alignment we use a kinematic mount for the second mirror after the spatial filter. The kinematic mount consists of two parts, a magnetic baseplate, on which the optical component is mounted, and its counterpart, which is screwed down onto the optical table. This kind of mounting has the advantage that the base has a reproducible position with respect to its counterpart. When the mirror is removed, it is usually relatively easy to put it back into nearly the same position, so that only minor realignments are necessary.

At the beginning of the setup for recoil-induced resonance experiments, a telescope is included to change the beam width of the Ti:sapphire beam. A 250 mm lens and a 125 mm lens are used to halve the beam width because this optimizes the diffraction efficiency of the acousto-optic modulators that follow in the setup.

One of the main goals of our setup is to produce two beams with a relative frequency stability better than 100 Hz. This is only possible by using one laser, splitting the beam into two parts, and modulating the frequency of both beams separately. Because a laser is coherent, this procedure can produce frequency differences that are stable, although the linewidth of the

laser is approximately 10 MHz. We work in a far enough detuned regime that the small overall jitter in frequency is of no importance. A 50% beamsplitter is used to produce two beams with approximately identical intensity. Because the Ti:sapphire laser puts out vertically polarized light, and the beamsplitter works appropriately only for horizontal polarization a half-wave plate is included to rotate the direction of polarization.

The power in one of the two beams is recorded during the measurement. This beam is referred to as the "probe" beam, while the other beam is called the "pump" beam. Note that this is only a convention, and in principle nothing distinguishes the roles of the two beams in the experiment, except one is monitored on a photodiode. Having shown how to produce two beams with identical frequency and approximately the same intensity, we now continue to describe the manipulation of the beam frequencies.

It is difficult to shift an optical frequency on the order of only hundreds of kHz with any device. We therefore use an acousto-optic modulator in each beam and the fact that the relative frequency shift of two AOM's can be controlled very precisely (Section 5.2). First, let us follow the probe beam, which passes the beam splitter without being deflected. A long focal length lens ($f = 750$ mm) is used to slightly focus the beam through the acousto-optic modulator (denoted by AOM2 in Fig. 5.1), which is placed approximately at the focal plane. The AOM2 is an IntraAction 80 MHz modulator (AOM-402AF3-10). The use of a long focal length lens optimizes the diffraction efficiency of this model. Here, we are primarily interested in the frequency shift of 80 MHz and not in the fact that the AOM deflects the first order

light. We use the -1 diffraction order so that the frequency after the acousto-optic modulator is shifted down by (80000.00 ± 0.05) kHz due to the RF drive (Appendix B and Section 5.2). The remaining zeroth order light is blocked. The efficiency of the acousto-optic modulators in the recoil-induced resonance experiment is discussed along with the driving electronics in Section 5.2.

Half of the frequency-shifted light is deflected into a photodiode by another beam splitter, and half of the light propagates to the interaction vacuum chamber (Section 4.1). The light heading for the diode is slightly focused down onto it by a 200 mm lens. The signal from the diode is used as a reference signal to distinguish between uncorrelated fluctuations in the light intensity and the signal due to the light-atom interaction (Sections 5.2 and 5.4).

After collimating the interaction beam with a 1000 mm lens, resulting in a slightly expanded beam, a second telescope is included (see Fig. 5.1) to reach the final beam width of (0.70 ± 0.01) mm before the chamber. At this point a second spatial filter can be included to clean up the mode structure of the beam that might be disturbed by the previous optical components. Usually, no spatial filter is included because its alignment is time consuming and the mode structure of the incoming beam is sufficiently close to a pure TEM_{00} mode.

The frequency shift of the second beam is accomplished by double-passing an IntraAction 40 MHz modulator (AOM-402AF3-10). Double-passing can be accomplished using a polarizing beamsplitter. The horizontally polarized light propagates through it without being deflected and is focused through the AOM with a 400 mm lens. The zeroth order is blocked by an iris. The

40 MHz down-shifted light in the -1 diffraction order propagates through a quarter-wave plate, is reflected by a 400 mm radius concave mirror and reflected back on the same beam path. This arrangement results in a rotation of the polarization axis by 90°. The light is therefore vertically polarized when it passes again through the AOM and is shifted down again by the same amount in frequency. The driving frequency of this AOM is swept during the experiment. This sweep results in the stable but time-dependent frequency difference between the two beams discussed in Sections 5.2 and 5.3. The polarizing beam splitter deflects the vertically polarized light, as shown in Fig. 5.1, and the rest of the setup in front of the chamber is equivalent to that of the probe beam. Only an additional half-wave plate is included in order to return to a horizontally polarized beam. This ensures that the two recoil-induced resonance beams have the same polarization in order to avoid the complications introduced at the end of Section 3.3.2.

The two beams are brought up to the level of the vacuum chamber by periscopes consisting of a number of mirrors. In contrast to the simplistic picture shown in Fig. 5.1, the two beams enter the chamber in a vertical plane at an angle of $(5.5 \pm 0.2)^\circ$. This angle is measured by projecting the two beams on the wall approximately 2 m from their intersection point and measuring their spatial distance. The mounting of the mirrors deflecting the beams into the chamber sets severe restrictions on that angle. Therefore, we have not been able to investigate the scaling of the recoil-induced resonances with this parameter. The beams propagate at a small angle relative to one of the trapping beams and use its windows to enter and leave the chamber. Each beam is focused down by a 300 mm lens, and the two beams intersect

in the focal plane at the atomic cloud (Section 5.1.2). There, the beam width can only be estimated by the theory of Gaussian beam propagation because it naturally cannot be measured inside the vacuum chamber. This estimate yields a beam width of 0.12 mm and is comparable to the width of the atomic cloud of 0.15 mm.

After leaving the chamber the pump beam is simply dumped. A 250 mm lens is chosen to focus the probe beam slightly down onto a second photodiode (Section 5.2) while a periscope is used to send it down to the table again. This diode takes the actual recoil-induced resonance signal (Section 5.4) and completes the basic setup for the recoil-induced resonance experiment.

Nevertheless, there are several components that have to be inserted additionally for different measurements when the parameter space of detuning and beam power is explored. Because of an electronics problem (Section 5.3), the intensity of the Ti:sapphire beam cannot be reduced below 3% by AOM1. To reduce the intensity further in several measurements, additional beam splitters are inserted either before the 50% beamsplitter to reduce the power in both beams or behind the beam splitter to reduce the power in only one of the beams. We tried to reduce the power using the drivers of AOM2 and AOM3, but this resulted in a higher noise level (Section 5.2), so that we used the beam splitters. With this combination of AOM1 and the beamsplitters we varied the intensities between 0 and 35 mW in the pump beam and between 0 and 3 mW in the probe beam.

To change the polarization direction of the probe, a half-wave plate can be inserted directly in front of the last 300 mm lens in front of the cham-

ber. Experiments with a circularly polarized pump beam are performed with an additional quarter-wave plate before sending the pump beam up to the chamber. For experiments in a polarization spectroscopy setup (Section 6.3), crossed polarizers are inserted. One is placed between the 300 mm lens and the $\lambda/2$ plate in front of the chamber in the direction of the incoming light, and the other one is placed directly behind the chamber.

5.1.2 Alignment

The alignment of most of the optical components is straightforward. Only the alignment of the acousto-optic modulators, the spatial filter, and the photodetectors, and the process of intersecting the laser beams at the location of the atomic cloud have to be considered in detail. The alignment of the Ti:sapphire laser is very involved and beyond the scope of this thesis. The reader is therefore referred to Klappauf [12].

Because the wavelength of the cesium D_2 line is in the near-infrared (852 nm), special equipment has to be used to visualize the beam while aligning the setup. For this purpose IR-cards based on fluorescence or hand-held IR viewers based on a cathode-ray tube are useful.

The alignment of an acousto-optic modulator begins with focusing the beam onto the aperture of the device so that the beam propagates through it without clipping. The focal length of the focusing lens is determined by optimizing the AOM's diffraction efficiency. Because the AOM is based on Bragg diffraction (Appendix B), the angle between the traveling sound wave inside the AOM crystal and the incoming light is of crucial importance. It is

easiest to use a rotational stage for mounting the modulator. One can then rotate the device, including the traveling sound wave, until the diffraction in the plus or minus first order is optimized. If no rotational stage is at hand a normal mount with a spring-loaded thumbscrew also works. A standard power meter can be used to monitor the efficiency while aligning the AOM when the zeroth order is blocked. The rotation can misalign the beam and lead to clipping, so that an iterative process must be used. Once the input angle is optimized the vertical angle with respect to the crystal can be optimized by monitoring the diffraction efficiency with a power meter.

Because an acousto-optic modulator can shift the frequency either up or down by the specified amount, one has to make sure that the right order is used just by looking at the geometry of the AOM. In our setup it is of special importance that AOM2 and AOM3 diffract into the same order because the frequency difference in the recoil-induced resonance experiment must be swept near zero.

The double-passed AOM is aligned in a similar way as for a single-pass setup. The second pass is especially easy to align because one only has to reflect the beam back onto itself with the concave mirror. If the first pass is optimized the second pass is automatically optimized as well because Bragg diffraction works equally well in both directions (Appendix B).

A spatial filter is most easily aligned by inserting it slightly away from the focal plane of the focusing lens on a three-dimensional translation stage. The pinhole has to be moved around until a little light propagates through. Then, the spatial filter can be moved towards the focal plane while recenter-

ing the pinhole in the other two dimensions by maximizing the power going through. When the focal plane is reached, the transmitted power is maximized, and the diverging beam should be visible as a round spot with several diffraction rings when projected on a screen. A more tightly focused beam results in less attenuation, but the cleaning process also becomes less efficient.

The correct alignment of the two photodiodes measuring the intensity of the probe beam, is particularly important because it can dominantly affect the noise level in the experiment. The beam size has to be smaller than the active area of the photodiode. If part of the beam is clipped, tiny spatial fluctuations in the beam will lead to a large noise level. The same is true if the beam is too tightly focused onto the photodiode, because the sensitivity of the active area is not perfectly uniform. Therefore, the focusing lens has to be chosen carefully, and the beam spot has to be as centered on the active diode area as possible.

Finally, one has to make sure that pump and probe beam intersect at the position of the atomic cloud at a well defined angle because otherwise all our theoretical considerations in Chapter 3 are useless for predicting experimental results. The atomic cloud, while trapped in our magneto-optical trap (Chapter 2), can be monitored with a survey camera that is sensitive in the near infrared and visualizes scattered light from the cooling and repump beams. Hitting the atoms with an intense, additional beam (> 0.5 mW) results in a visible distortion of the MOT with a clear maximum when the beam is centered. Blocking one of the beams at a time and aligning the other by moving the beam over the window of the chamber until the MOT is deflected

has proven to be a reliable alignment method. When both beams are aligned in this way, no problems occurred during the experiment due to the beam alignment. A slight variation in the alignment, i.e., missing the point of maximum distortion, can result in an uncontrolled decrease in the available intensity at the position of the atoms. Repeated alignments usually seem to lead to slight variations in the intensity at the atoms (Section 6.2.1).

5.2 Electronics

The electronics used in the recoil-induced resonance experiment can be divided into three large groups. First, the components that control the frequencies of the two recoil-induced resonance beams are discussed in Section 5.2.1. They have to provide the short linear sweep of the two beams' relative frequencies with great precision in order to make the investigation of the resonances possible. Second, the electronics used to measure the intensities in the probe beam and also to manipulate this data before it is recorded by a digital scope are self-made and discussed in greater detail in Section 5.2.2. Their main feature is to extract the small expected signal out of the large background. Third, there are the electronics controlling the timing of the whole experiment and used to produce our cold atoms. Their discussion is postponed until Section 5.3 because they are introduced most easily when the timing itself is discussed.

5.2.1 Frequency Control Electronics

The frequencies of the two recoil-induced resonance beams are controlled by the acousto-optic modulators introduced in Section 5.1.1. Because the frequency shift due to these AOM's simply equals their RF input (Appendix B), we have

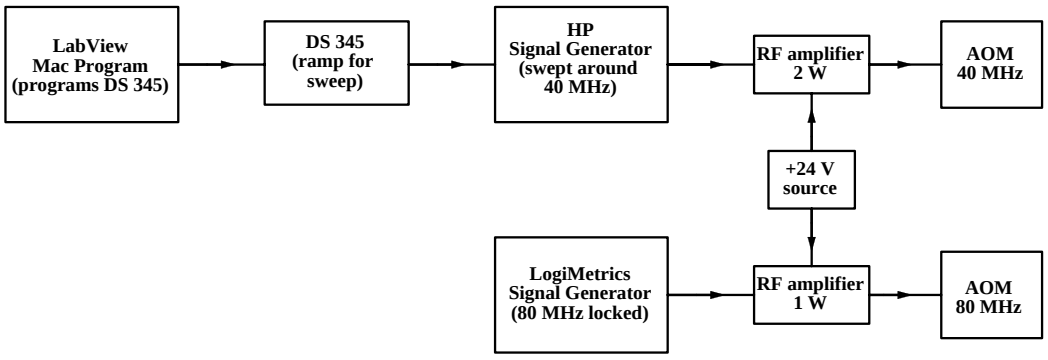

Figure 5.2: Electronics for frequency control. The arrows show the flow of signals from an output of one device to an input of another one.

to discuss how these RF signals are generated. A schematic of the control electronics discussed below is shown in Fig. 5.2.

The single-passed AOM for the probe beam is driven by a LogiMetrics (Model 925 S 125) Signal Generator. This RF source includes an internal counter that proves to be sufficiently precise (better than 100 Hz at 80 MHz) by comparing its readings with those of external, high-precision counters. The output can be set to exactly 80 MHz ($\pm$100 Hz) and phase-locked such that it is stable and does not vary for hours. When the signal generator unlocks, it usually jumps significantly and has to be reset completely. The LogiMetrics output is amplified by a Mini-Circuits 1 W RF amplifier (ZHL-3A) driven by a standard 24 V current source. If the input signal level of the amplifier exceeds +2 dBm, it starts to saturate and the output signal is not a clean sinusoidal wave. Therefore, the output of the signal generator is set to +2 dBm. The 1 W output of the RF amplifier is directly connected to the acousto-optic modulator and leads to a diffraction efficiency of only 25% because it is significantly

lower than the specified input power of the AOM. Increasing the input level of the amplifier increases the diffraction efficiency at cost of the sinusoidal RF structure. Because more than enough power is available in our experiment we operate the LogiMetrics driver at +2 dBm. Reducing the output further to decrease the interacting light intensity in the chamber (Section 5.1.1) leads to large power fluctuations in the first-order diffracted beam (i.e, noise) and must be avoided.

The double-passed AOM for the pump beam is driven by an HP 8640 B signal generator. It includes an internal counter that is as reliable as in the LogiMetrics device and is operated at around 40 MHz. The HP's frequency modulation input is used to sweep the output frequency. A sweep in voltage at the input from zero to one volt results in a sweep in frequency from 0 up to 320 kHz, starting from a set frequency. To use the full range of the DS345 function generator producing the linear ramp for the sweep (-5 to +5 V), a circuit is included between the DS345 and the frequency modulation input that adds 5 V to the input voltage and divides it by ten. The generation and timing of this ramp for the frequency sweep is discussed in detail in Section 5.3 along with all the other function generators used during the experiment. In this swept mode the signal generator cannot be phase-locked, but it is nevertheless stable. The frequency varies by less than 1 kHz per minute, which is unimportant for our experiment on a 1 ms timescale. The frequency varies linearly with input voltage within the accuracy of our measurement method (see Fig. 5.3). The measurement in Fig. 5.3 is taken in steps, i.e., no real sweep is applied, because any counter needs some time to measure the frequencies. However, the response time is negligible on the timescale of our experiment,

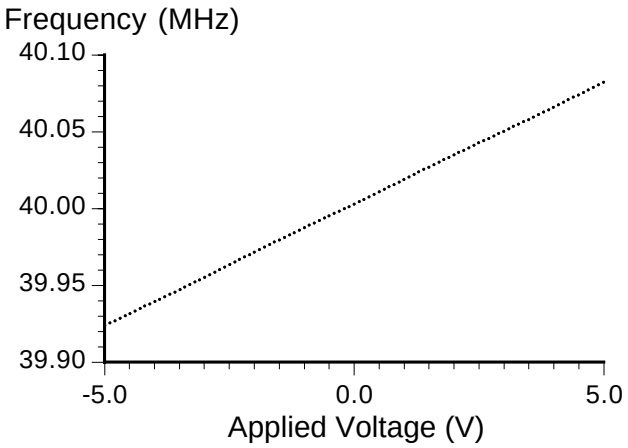

Figure 5.3: The frequency sweep. The output frequency of the RF generator varies linearly with the output voltage from the function generator, which provides the linear ramp for the sweep. The sweep is shown for the parameters used for all the data presented in Chapter 6. A linear fit results in (15.85 ± 0.05) kHz/V.

as can be seen on a digital scope. The output of the HP signal generator is amplified by a Mini-Circuits 2 W amplifier (ZHL-1-2W). The response time of the amplifier is also negligibly short. We drive the HP with an output power of +2 dBm because the same considerations as for the other Mini-Circuits amplifier apply. The diffraction efficiency of the double-pass is usually 25% and sufficient for our purpose. Note that in a double-pass the applied input frequency at the AOM is doubled in the outgoing light beam. Therefore, a sweep of ±50.0 kHz around 40000.0 kHz results in a beam swept ±100.0 kHz around 80000.0 kHz. Measuring the beat note in a heterodyne between the two beams in our setup shows that a linear sweep of the HP input voltage results in a linear dependence of the frequency difference as expected.

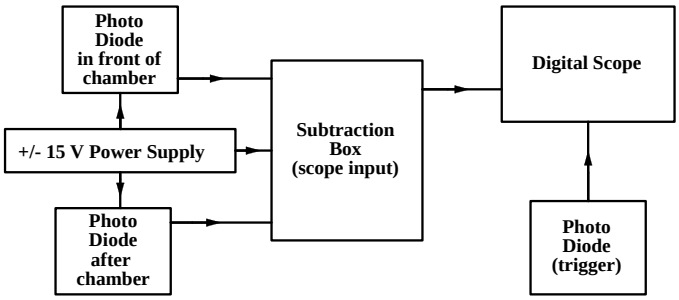

Figure 5.4: Electronics for taking data. The arrows show the flow of signals from an output of one device to an input of another one.

5.2.2 Measurement Electronics

In a recoil-induced resonance experiment, one expects a tiny signal (usually less than 1%) on top of a large background. In other words, the noise in the laser amplitude can be bigger than the signal we want to measure. To get rid of these fluctuations, which are unfortunately partly on the same timescale as the expected signal (several kHz), we measure the intensity in the probe beam in front of and behind the chamber and subtract the two signals with an analog subtraction box. A schematic of the setup for the data-taking electronics is shown in Fig. 5.4.

To record the power in the two beams we used S-1226 photodiodes with the photocurrent to voltage converter circuit shown in Fig. 5.5. This circuit has an output voltage of (3.0 ± 0.2) V/mW and the diode is linear up to an overall input power of 1.5 mW. The noise at frequencies above 1 kHz is approximately (0.3 ± 0.1) mV, for the case where no light is impinging on the diode's sensitive area, and increases only slightly for higher input powers. If a fraction of the Ti:sapphire laser power that is typical for our experiments is incident on the

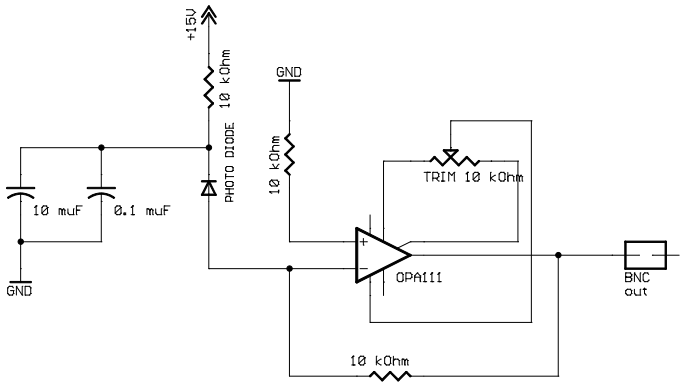

Figure 5.5: Schematic of the used photodiode circuits. An operational amplifier is used to convert the photocurrent into the output voltage.

diode, the noise in the light power clearly dominates. More problematic is the pick-up noise of 60 Hz and its harmonics. Because of ground loops, this part of the noise can be as big as several mV. Fortunately, the timescales of this noise and the timescale of the signal are so different that our analysis procedure can suppress it reasonably (Section 5.4).

The diode has a rise time of approximately 4 μs. The width of the resonances (time difference between the two peaks) when the experiment is driven with our typical parameters (Section 5.3) is usually around 30 μs. Therefore, we are not working too far from the limitations of our electronics. This point should be kept in mind when we analyze the data in Chapter 6. The circuits are made for driving high impedances and should be connected on an input in the MΩ range (not to a 50 Ω input).

The schematic of the subtraction circuit is shown in Fig. 5.6. The two input signals to be subtracted can be scaled using the two potentiometers and the two OPA111 operational amplifiers on the left of the schematic. This

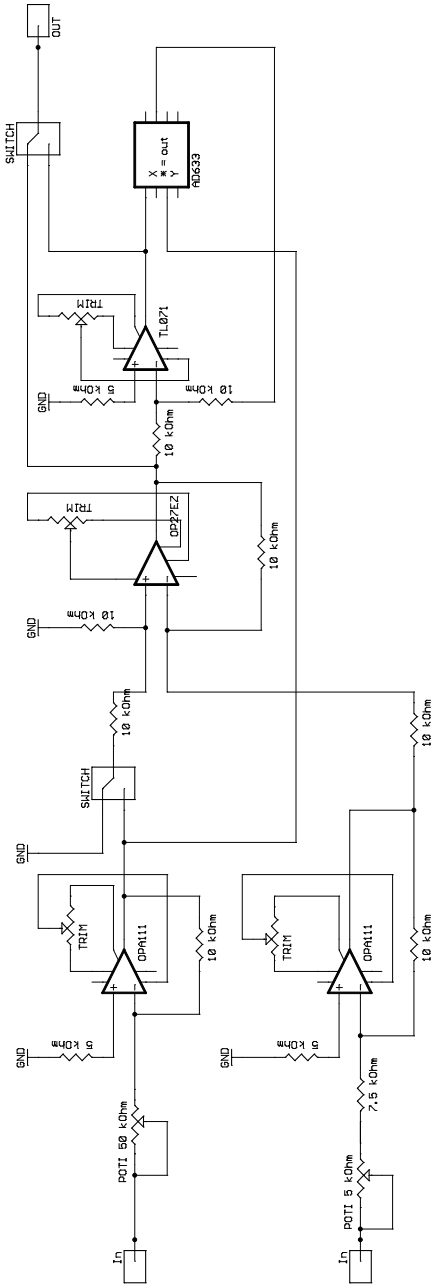

Figure 5.6: Schematic of the subtraction circuit. The two input signals can be scaled, subtracted and the output can be normalized.

adjustment is convenient because the signal levels of the two diodes connected to the subtraction box are in general not completely equivalent. The OP27 operational amplifier subtracts either the second input signal or ground from the first input signal, so that it is possible to look at only the first input signal instead of the subtracted signal. Finally, the TL071 operational amplifier and the AD633 multiplier offer the opportunity to normalize the output with respect to the second input signal.

Due to the potentiometers used to scale the incoming signals, the subtraction circuit deforms signals above 100 kHz, and so a reliable measurement below the 10 μs timescale becomes questionable. With increasing frequency, the output amplitude of a sine wave with the same input amplitude rises until 400 kHz is reached. There, the input level is approximately doubled in the output. At around 400 kHz the output amplitude decreases and drops to zero at 2 MHz. So, we are taking data near another limit of our electronics.

Again, we have to consider two different kinds of noise. Most of the observed noise is 60 Hz noise and higher harmonics. This noise can reach the 5 to 10 mV level but the different timescale compared with our data helps to suppress this noise (Section 5.4). Most of the higher frequency noise is noise beyond 500 kHz and can be suppressed with an additional RC low pass that suppresses 300 kHz noise by a factor of two.

The overall remaining noise level in the data due to the electronics is 0.3 mV without any light on the diodes. The laser noise can be suppressed via the subtraction by a factor of approximately 20, so that an intensity of 0.1 mW on each diode does not lead to a significant increase in the noise. At

higher powers the noise increases linearly with laser power and reaches 3 mV at 1.0 mW incident power on each diode. Without any subtraction the signal-to-noise level would certainly drop to about unity for small laser intensities and below unity for higher intensities. Therefore, the subtraction circuit is an absolutely necessary tool.

At this stage of the experiment an additional normalization of the output signal using the included multiplier makes no sense because even a perfect normalization would be invisible within the remaining noise. Furthermore, because the multiplier part of the circuit leads to additional noise, we do not use this option.

The output signal of the subtraction box is connected to one of the digital scope channels (1 MΩ impedance). A Tektronix TDS 524A digital scope is used in our experimental setup. All the important settings are computer controlled and programmed before each experiment starts. One can therefore accomplish, for example, different interaction times and/or expected signal levels. The start of the measurement sequence is triggered by the transient produced by the third photodiode in the setup when the light is turned on (see Section 5.3 for details on the timing).

5.3 Timing

Here, we consider the timing of our experiment, which is of crucial importance. Because the timescales in atom optics are short, the timing must be very precise. The whole experiment can be divided into several steps. First, the cold atoms have to be produced in a MOT (Section 5.3.1). Then the atoms

are released so that they are free. At this point, the recoil-induced resonance experiment takes place (Section 5.3.2). After a certain free drift-time the CCD camera is used for the time-of-flight analysis of the momentum distribution. At this point the atoms are again hold in place in an optical molasses (Section 5.3.3).

The timing of the experiment is computer controlled. A LabView program is used to program several pulse and arbitrary wave form generators and sets the main trigger to start the experiment. Furthermore, the computer is used to directly control the magnetic trapping field.

For the high precision timing in the experiment, we use two Stanford Research Systems DG535 pulse generators. One of the options of the DG535 is that it can produce one pulse with variable intensity and one TTL pulse with a timing precision of a few ps at any time in the experiment. Each pulse is specified by a starting and an ending time after a trigger pulse. The DG535 has a lower output limit of 10 mV. Because of this property, we are not able to have full electronic control over the intensity in the recoil-induced resonance beams as discussed in Section 5.1.1.

For control signals more complicated than a simple pulse, the experiment requires the use of Stanford Research Systems DS345 arbitrary wave form generators. Here the timing is a little less precise but the wave forms can be programmed point by point (16,299 points altogether) and have a resolution of 100 ns.

The signals generated in this way control all the important parameters of the experiment. First, the light intensities of the trapping, repump, and

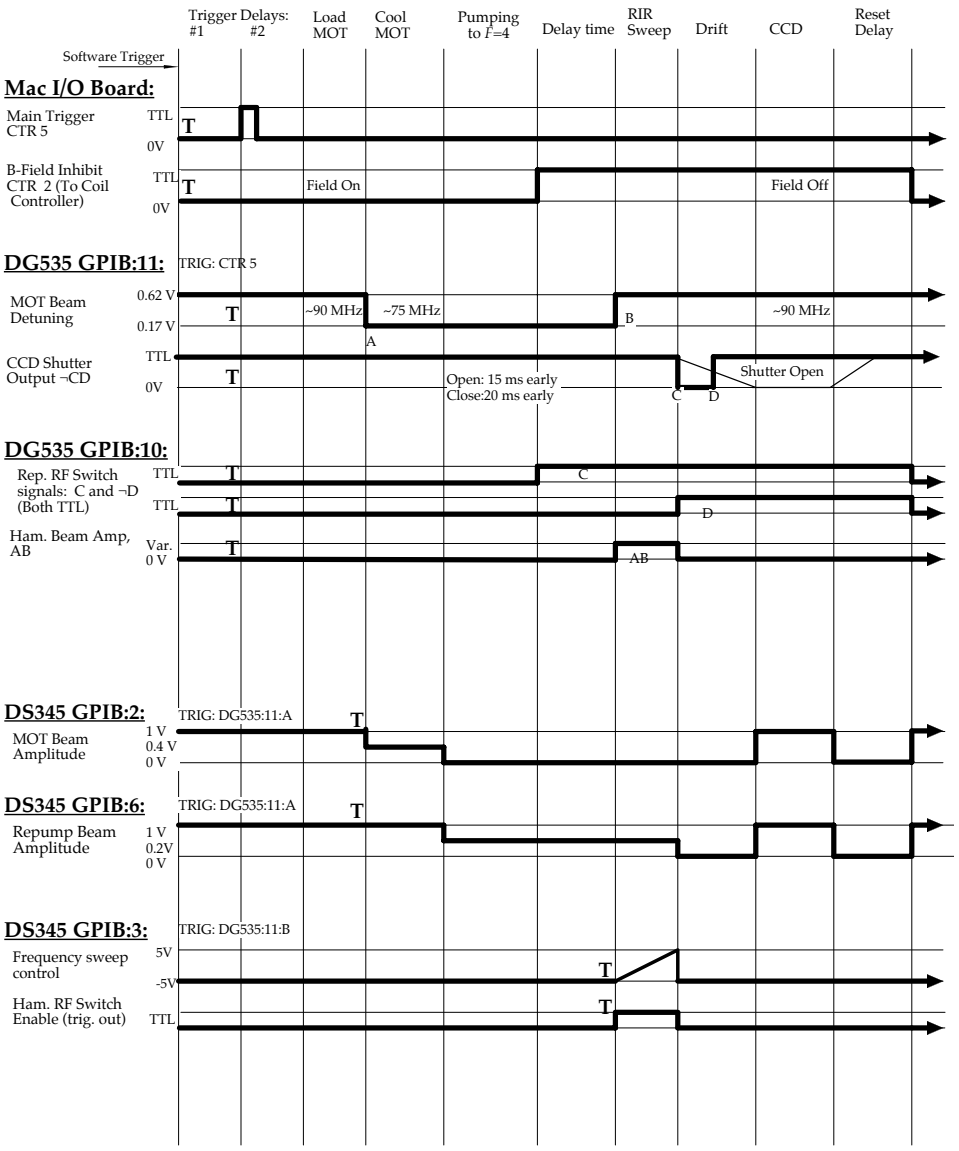

Figure 5.7: Timing diagram of the experiment. The different signals produced by the pulse and function generators are shown. The T's show where the programmed output of each device is triggered.

interaction beams are controlled via the amplitude modulation input of the AOM drivers for the different beams. The signal controls the input RF power for the AOMs and therefore the light intensity in the first diffraction order that is used in the experiment (Appendix B). Second, the detuning of the trapping beams is controlled by the frequency modulation input of the corresponding AOM driver. This modulation works in the same way as the modulation of the frequency in one of the recoil-induced resonance beams (Section 5.2.1). Third, RF switches are controlled by TTL-signals. These switches (when set to the off position) are used to block any residual driving power for the acousto-optic modulators controlling the repump and recoil-induced resonance beams. This is necessary because even at zero amplitude the drivers put out enough power that a small amount of light is diffracted into the first order and disturbs the experiment. Fourth, the magnetic field of the trap coils is switched on and off with a TTL-signal that is converted by the box driving the anti-Helmholtz coils. Fifth, the shutter of the CCD-camera is also controlled by a TTL-signal. Finally, the frequency sweep of one of the recoil-induced resonance beams (Section 5.2.1) is controlled via a linear ramp signal (from a DS345) connected to the frequency modulation input of the HP RF generator. Fig. 5.7 shows the timing diagram of the recoil-induced resonance experiment, including the time dependence of all important signals.

5.3.1 MOT Timing

Before the experimental time sequence starts, the MOT beams are at full intensity. The magnetic field is also applied, so that a magneto-optic trap is established. Because the programming of all the function generators leads

to unpredictable signals before the actual experiment starts a 7 seconds time interval is included at the beginning where the magneto-optical trap loads itself with atoms. This ensures the independence of the following experiment from the time before. During this time the trapping light is detuned by 18 MHz. Increasing the trapping beam detuning to a value of roughly 55 MHz (by setting the value in the program) and decreasing the intensity of the beams for 1 ms results in further cooling the atoms. At the end of this time interval the trapping beams are turned off completely. Now, the repump operates alone for 0.25 ms with reduced intensity. This results in a final pumping from the $F = 3$ into the $F = 4$ hyperfine ground state. Because the Raman transitions driven by our laser frequency only couple to the $F = 4$ state this pumping is of crucial importance. After this repump interval the voltage supply for the trap coil current is turned off, and the magnetic field starts to ring down. These conditions allow a free drift of the atoms. The repump is still incident on the atoms but it is far-detuned and should not have large impact on the free motion of the atoms in the $F = 4$ ground state. Only if spontaneous scattering events lead to a population of the $F = 3$ state does the repump become important, in which case it brings those atoms back into the $F = 4$ state. Because we are only measuring the $F = 4$ momentum distribution, we can assume that the impact of the repump on this measurement is small. Therefore, at this point the initial conditions for a recoil-induced resonance experiment are fulfilled. We have produced a freely propagating, relatively dense cesium cloud (approximately 10^6 atoms within 10^{-3} mm^3 volume) with a temperature usually around 10 photon recoils.

5.3.2 Timing of the Experiment

After 1 ms of free drift the actual experiment begins. The magnetic field is still ringing down and can lead to complications. The actual strength and gradients of the magnetic field are not precisely known because they are extremely hard to measure. However, delaying the start of the experiment longer is not possible because the freely drifting atoms move gradually out of the laser light.

The recoil-induced resonance light is turned on by enabling the corresponding RF switch and turning up the RF output of the driver of AOM1 to the desired value. When the light comes on, the transient produced by the first photodiode in the setup (shown below the Ti:sapphire laser in Fig. 5.1) triggers the digital scope. Simultaneously, the linear ramp for the frequency sweep is started. The sweep time and the frequency range are variable and can be set in the controlling program. Only the starting frequency for the sweep and the coarse frequency range have to be set on the HP signal generator. Usually the whole sweep is 320 kHz over 500 μs.

This is the time when the interaction leading to the observed recoil-induced resonances takes place. The scope is automatically set to record this time interval with the best possible resolution (15000 points). After this short time interval the light in the recoil-induced resonance beams is shut off completely. The amplitude settings of the AOMs controlling the frequencies of the two beams is not changed. They are running during the whole experiment and therefore their rise time is of no importance.

After the measurement interval, the repump beam is shut off by setting the output amplitude on the AOM driver to zero. Furthermore, its RF switch

is disabled to completely shut off the light in the first diffraction order.

5.3.3 TOF Timing

After the interaction took place the atoms are again freely drifting in the dark. During the next 15 ms they convert their different momenta into distance making a time-of-flight measurement possible. At the end of this time period the atoms are held in place in an optical molasses. The MOT lasers are turned on and create the "sea of photons" that holds each atom in place while the shutter of the CCD-camera is open to take a picture of the expanded (according to its free drift) atomic cloud. Because of electronic delays the signals for opening and closing the shutter have to be sent much earlier than the actual exposure time (see Fig. 5.7).

When the shutter closes, the experiment is over. The lasers are turned off for a short time before the whole experiment is reset. Then all parameters are back to their initial values at the beginning of the experiment.

5.4 Analysis

In this section we describe the analysis of the experimental data, which is read out of the scope and the CCD camera by a computer. The computer automatically extracts the momentum distribution from the CCD picture. This time-of-flight analysis is equivalent to the procedure in all cesium experiments in our group and is briefly described in Section 5.4.3. The raw recoil-induced resonance lineshape and the momentum distribution as extracted from the TOF method are saved permanently into a file. We use the methods discussed

in Section 5.4.1 to remove most experimental artifacts from the raw lineshapes, before we analyze the data, as described in Section 5.4.2.

5.4.1 Noise and Background Suppression

The raw data, as recorded by the digital scope in a single run of the experiment, pose essentially two problems. First, in spite of our efforts to reduce the noise with our analog subtraction (Section 5.2.2), the data are relatively noisy. Second, a timing problem in the subtraction box and the large 60 Hz pick-up noise lead to a nonzero, time-dependent background.

One simple but quite effective method in noise suppression is to measure more than once and average the data. We average up to 25 experimental runs. This reduces the high frequency noise by a factor of 5-10. The main disadvantage of the averaging method is that it is time consuming. Including the programming of the function generators, the whole measurement cycle takes approximately 45 seconds. Moreover, the requirement of multiple runs destroys the possibility of *in situ* measurements of the momentum distribution. Figure 5.8 shows the raw lineshape after averaging over 25 measurements.

While suppressing the noise effectively, averaging the data cannot overcome the background problems. Due to the timing problems in our subtraction circuit there is a large peak when the laser beams are turned on. At later times during the experiment, the background looks like the tail of an exponential. This signature is very reproducible. Repeating our experiment, but sweeping near 1 MHz off resonance rather than through the resonance results in a lineshape as shown in Fig. 5.9. This data is equivalent to the signal in the

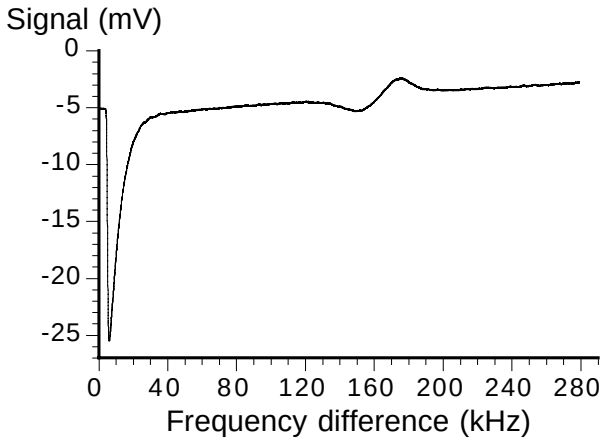

Figure 5.8: Raw data as measured in a recoil-induced resonance experiment. There is a clearly visible resonant structure. The x-axis shows the frequency difference of the pump beam to some reference frequency.

recoil-induced resonance experiment except that the resonant structure itself is missing. Therefore, this signal can be subtracted from the signal that includes the recoil-induced resonance to eliminate the background. It is necessary to average the background as well before subtracting it from the signal, because otherwise the improvement in signal-to-noise we gained by averaging the signal is lost.

Another problem is that there is a small, non-reproducible, overall offset in the measured voltage in each experiment run. It is most likely due to small drifts in our subtraction circuit. If the scaling of the input signals within the subtraction box (Section 5.2.2) varies only by one percent, there is a resulting overall offset of a few mV because the two input signals are not perfectly balanced any more. The signal is also perturbed by roughly one percent, but this variation is unimportant compared with the noise. Even after averaging the signal and the background over several measurements, a small constant

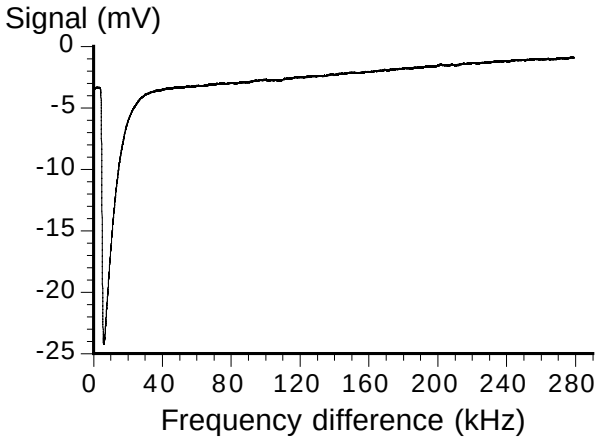

Figure 5.9: Background signal. The same experimental parameters as in Fig. 5.8 are used except that the frequency difference of the recoil-induced-resonance beams is not swept through zero. The data has the same structure as the data in Fig. 5.8 but the resonance is missing.

offset in the background-subtracted signal remains (compare the graphs in Figs. 5.8 and 5.9).

To eliminate the small offset we fit a constant to the background-subtracted signal and subtract it from the data in order to get a well defined zero line. Figure 5.10 shows the central part of the lineshape in Fig. 5.8 with the recoil-induced resonance, in the final, background-free form, which is used for the analysis.

5.4.2 Extracting the Momentum Distribution

Our data-taking electronics are set up in a way that gain or loss in the probe beam reflects itself in a positive or negative voltage, respectively, in the output of the subtraction box. Because we sweep the pump frequency around the probe frequency, the frequency difference between probe and pump decreases

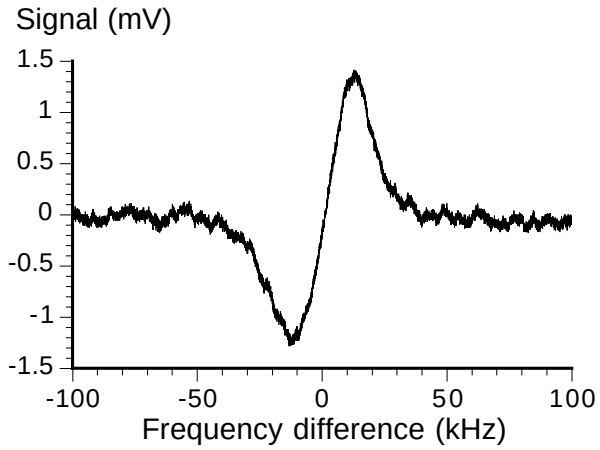

Figure 5.10: Background-free lineshape. The central part of the data shown in Fig. 5.8 is shown after the background is subtracted as described in Section 5.4.1. Here, the x-axis shows the frequency difference between the pump and the probe beam.

linearly and we expect an inverted derivative of a Gaussian lineshape (see Fig. 5.10).

The first step in the analysis is to assign an appropriate frequency to each point in the column of data points, which is produced by the scope and read by the computer. In other words, the point number (1 - 15000) is multiplied by the time interval between the points (0.04 μs/point in most of our experiments) and the sweep rate ($\approx$ 640 kHz/ms in most of our experiments). The x-axis then shows the difference in the frequency of the pump beam with respect to some reference value (see, for example, Figs. 5.8 and 5.9). Because the sweep begins slightly after the first data point is taken, the frequency axis is not exactly correct for the very first part of the graph. However, these first data points do not contain valuable information anyway. The frequency assigned to each point is shifted by roughly half of the sweep range of the experiment

relative to the difference in frequency between the pump and probe beam. It is hard to determine exactly the point of zero frequency shift from the sweeping parameters alone without analyzing the signal, because of electronic delays on the order of several μs (corresponding to an uncertainty of several kHz in frequency difference).

If the signal is the derivative of a Gaussian, as theory predicts for a thermal atomic cloud, one can find the point of zero detuning during the measurement from theoretical considerations. It must be the center of the resonance, where the lineshape crosses the zero signal level. In Fig. 5.10, this knowledge is used to label the x-axis appropriately. For parameters where the signal is not a derivative of a Gaussian (or the derivative of another symmetric momentum distribution) (Chapter 6) the zero detuning cannot be found in this way. Nevertheless, the sweep and the electronic delays do not change when the sweep parameters stay the same. In this case, the point of zero detuning is simply the same as for a measurement yielding a Gaussian distribution.

The scale of the x-axis can be converted to the momenta of the atoms (measured in multiples of a photon recoil $\hbar k$) coupled resonantly at each point of the graph using Equation (3.29). With the wave vector of the cesium D_2 line ($k = 73714$ cm^{-1}), the mass of a cesium atom ($m = 2.2069 \times 10^{-25}$ kg), Planck's constant ($\hbar = 1.0546 \times 10^{-34}$ Js) and the angle between the beams ($\Theta = (5.5 \pm 0.2)^\circ$), the conversion factor between frequency and number of recoils ($2\pi m/(\hbar k^2 \Theta)$) turns out to be (2.52 ± 0.10) recoils/kHz. (Note that this number is multiplied by a frequency, not by an angular frequency, to yield the right result.) This conversion is an important step in extracting the

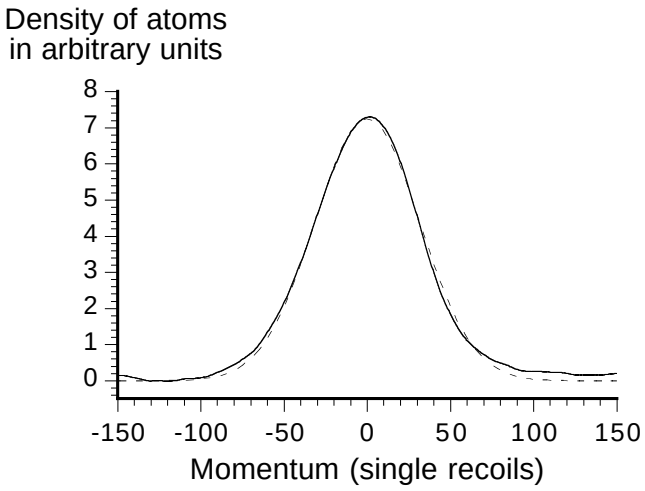

Figure 5.11: Example of a momentum distribution. The momentum distribution as extracted from the data in Fig. 5.8 is shown. The distribution is Gaussian and has a width of $\sigma_p = 30.3$ recoils. This width corresponds to a temperature of 182 μK. The significance of this temperature is discussed in Chapter 6.

momentum distribution from our data.

According to our theoretical analysis in Chapter 3, the signal is the derivative of the momentum distribution of the atomic cloud. To calculate the momentum distribution itself, i.e., the function we are interested in, we let the computer numerically integrate the measured lineshape after the background has been subtracted, as described in Section 5.4.1. The computer takes into account that our lineshapes are inverted derivatives and removes the inversion before the integration. Figure 5.11 shows the integrated version of the data shown in Fig. 5.10.

To extract the temperature out of a thermal distribution, we fit a Gaussian to the integrated data using a nonlinear fit routine in LabView. This fit

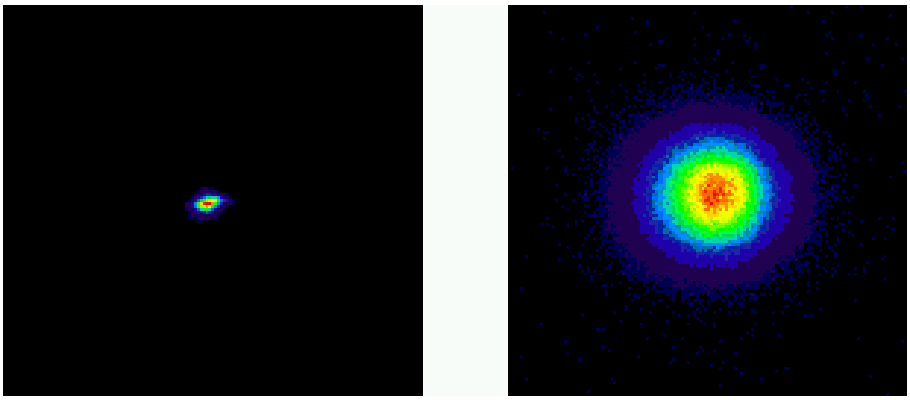

Figure 5.12: CCD-pictures of the atomic cloud. The left picture shows the initial cloud as produced in our MOT. The right picture shows the cloud after 15 ms of free drift. The momentum distribution can be extracted because the initial cloud of atoms is small compared with the expanded cloud.

yields the standard deviation of the distribution σ_p, which is connected to the temperature by

$$T = \frac{\sigma_p^2}{m k_{\mathrm{B}}}. \tag{5.1}$$

In other words, fitting a Gaussian to a thermal distribution measured via recoil-induced resonances reveals the temperature of the atomic cloud. Naturally, this method is only sensible when the distribution is thermal. Otherwise, one can measure the momentum distribution, but the notion of a temperature is not well-defined.

5.4.3 TOF analysis

The time-of-flight method relies on the fact that a momentum distribution is converted into a spatial distribution when the atoms are allowed to drift freely for some time. The atoms in a small initial cloud spread out, and after a time

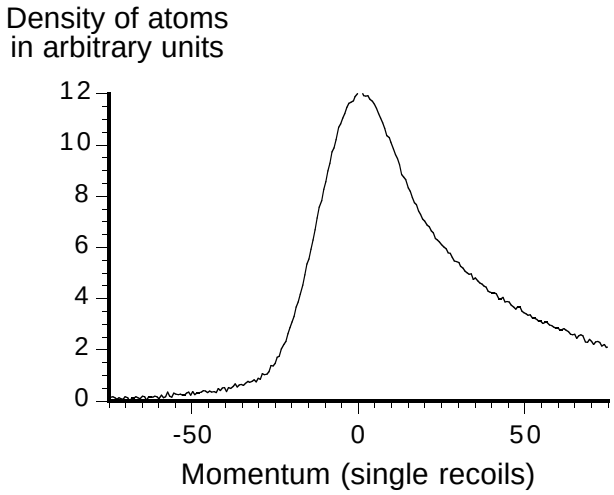

Figure 5.13: Momentum distribution from the time-of-flight analysis. The data shown in this graph corresponds to the same experiment as the data in Fig. 5.11. Clearly the momentum distributions are different in width as well as in shape. Note the significant asymmetry in the TOF momentum distribution. See Section 6.1 for a detailed discussion.

interval t, atoms with a momentum p are found a distance

$$x = \frac{pt}{m} \tag{5.2}$$

away from their initial position, where m is the mass of the particle. Our CCD-camera takes a picture of the atoms, and the amount of fluorescence produced by the atoms as a function of position results in a measure for the spatial density of atoms. The momentum distribution in one spatial direction is obtained by integrating the fluorescence at each point on one axis over the perpendicular direction in the 2-dimensional CCD picture. The resulting function, which depends on only one coordinate, can be transformed into the momentum distribution by Equation (5.2). If the atomic cloud is thermal, the temperature can be obtained by a fit to a Gaussian distribution. Figure 5.12

shows typical CCD-pictures of our atomic cloud before and after a free drift time of 15 ms. Figure 5.13 shows the momentum distribution as obtained by the time-of-flight measurement in the same experiment that lead to the momentum distribution shown in Fig. 5.11.

As for the recoil-induced resonance lineshapes the background in the CCD-picture is a real problem and a background picture with no atomic cloud has to be taken. Details on this background elimination and the analysis as a whole are discussed by Klappauf [12].

Chapter 6

Results

Having discussed the theoretical foundations of recoil-induced resonances and our experimental setup, we present and discuss the experimental data in this chapter. Section 6.1 is devoted to describing the general features of the data we obtained. Moreover, we discuss how our experimental setup limits our ability to further explore recoil-induced resonances and some as yet unresolved puzzles. Section 6.2 shows the effects of different beam intensities and detunings on the measured lineshapes. Finally, in Section 6.3, we describe the effects of different pump and probe polarizations and our attempts to perform polarization spectroscopy.

6.1 General Remarks

All the data presented here is obtained with the frequency difference between the pump and the probe beam swept between approximately -140 and +180 kHz during a sweep time of 0.5 ms (see Fig. 5.3). These parameters lead to the best signal-to-noise ratio. In this and the following section we restrict our discussion to a regime where the pump and probe are linearly polarized in the same direction (perpendicular to their plane of propagation).

One of the major drawbacks of our theoretical analysis is that it does not predict appropriate intensities of the recoil-induced resonance beams. It turned out to be a major task to find parameters that allow the observation of recoil-induced resonances at all. Using collimated beams with a waist larger than that of our initial atomic cloud (i.e., not including the two focusing lenses in front of the chamber) was not successful. Apparently, in the collimated configuration, the recoil-induced resonance signal is too small to be seen within the noise of our experiment. Unfortunately, the noise seems to increase more quickly with increasing intensities than the signal strength. The main problem is that most of the detected light is not interacting with the atoms, while increasing the noise and making the detection of the signal much harder. For example, beyond a certain probe beam power, beamsplitters must be used in order to reduce the power to a suitable level for the photodiodes. Naturally, the overall reduction of power also reduces the signal. Only a more sophisticated measurement method can overcome this problem (Section 7), if one insists on using large, collimated beams to provide a well-defined intensity at the atomic cloud.

A possible improvement in the direct power measurement in our experiment is to focus the beams so that practically all the light is interacting with the atoms. Because of the smaller beam waists, less overall power is needed to yield the same intensities at the atomic cloud. Lower power means less noise, and one may therefore hope to improve the signal-to-noise ratio. As a drawback of the focusing, the problems introduced in Section 3.3.1 can come into play. Moreover, repeated alignments seem to alter the effective intensity seen by the atoms (Section 6.2.1).

In the focused configuration (described in Section 5.1.1), we obtain lineshapes with the general structure of a Gaussian derivative, as expected from theory for a thermal cloud of atoms. Throughout our experiments, the measured lineshapes consist of one negative and one positive peak. The resonant structures are extremely narrow (several tens of kHz), and occur around zero relative detuning between pump and probe as theory predicts. (The uncertainty of our absolute frequency difference as mentioned in Section 5.4 is small compared to the width of the resonances.) Therefore, we can be confident that the lineshapes presented and discussed here correspond at least partly to recoil-induced effects. We therefore refer to the lineshapes as recoil-induced resonances. The scaling with intensities and detuning (i.e., with the effective Rabi frequency for the Raman transitions) does not follow the theoretical description and is investigated in detail in Section 6.2. Therefore, it is possible that other (not recoil-induced) effects contribute to the measured lineshapes (Chapter 5.4).

We now discuss some unresolved, fundamental problems in analyzing and understanding our data apart from the lineshapes themselves. First of all, the atoms should be pushed by the radiation pressure exerted by the pump and probe beams. Evaluating Equation (2.1) for the cesium D_2 transition [15] results in a scattering rate

$$\Gamma' = 67\ \mathrm{kHz}\Big(\frac{I}{\mathrm{W/cm^2}}\Big)\Big(\frac{\Delta_\mathrm{L}}{2\pi\cdot\mathrm{GHz}}\Big)^{-2}. \tag{6.1}$$

At the typical detuning of $\Delta_\mathrm{L} = 2\pi{\cdot}1.5$ GHz in our experiment this should result in roughly 15 spontaneous emission cycles per W/cm^2 during the 0.5 ms sweep. Therefore, the atomic cloud as a whole should be displaced by roughly

half a cloud diameter on the CCD-picture (see Fig. 5.12) per W/cm^2 pump beam intensity. Because of the tight focus of the beams, the intensities (particularly the pump intensity) can easily become as large as several W/cm^2. (With our beam parameters, the conversion factor from power to intensity can be estimated to be roughly 2 W/cm^2 per mW at the center of the Gaussian intensity distribution.)

A displacement of the atomic cloud as a whole is not observed at all, even at intensities higher than 10 W/cm^2. Only a diffuse halo of atoms leaves the atomic cloud in the direction parallel to the pump beam. One possible explanation is that the beams are more tightly focused at the position of the atoms than we think they are. In other words, only the central part of the atomic cloud is pushed by a visible amount while the other atoms "feel" only the fringes of the high intensity beam. This explanation is supported by the fact that all momentum distributions measured by the TOF method, after a recoil-induced-resonance sweep has been performed, show an asymmetry due to the interaction of the atomic cloud with the applied laser fields. In the propagation direction of the recoil-induced resonance beams, there are considerably more atoms with high momenta than in a thermal distribution (see Fig. 5.13). So at least a subset of the atoms shows the predicted pushing.

From the previous analysis, it is clear that we have not yet been able to work in a nondestructive limit. Even at the lowest powers where we can observe a signal, the intensity is at least as high as 2W/cm^2, and therefore the spontaneous emission is large enough to disturb the momentum distribution significantly during the whole measurement process of 0.5 ms. Only much

lower intensities would yield a less disruptive measurement. Unfortunately, our measurement technique is not sensitive enough to work in this regime.

Another puzzling fact is that the momentum distribution as obtained from the TOF data is not correlated to the intensities of the pump and probe beams. Since there are a different number of spontaneous emission cycles for different intensities the atomic momentum distribution should be heated more at higher intensities. We observe broadening, but it does not scale with the intensity of the two beams as expected. Usually, the broadening is on the scale of 6 photon recoils. However, even with the same parameters and no realignment of the beams, the broadening can fluctuate by up to 4 recoils. Moreover, higher intensities in the beam can lead to less broadening. This behaviour is completely unexpected. However, we can only judge the broadening by fitting a Gaussian to the time-of-flight data. Naturally, this procedure does not account for the asymmetry that is produced by the interaction with the recoil-induced resonance beams. If the beams are really focused at the center of the atomic cloud and the main interaction takes place with only part of the atoms, the behavior of the cloud as a whole could be rather different from our expectations.

In spite of these difficulties, our observed lineshapes are very consistent. Repeated alignments, according to the procedures described in Section 5.1.2, yield the same qualitative results. Only the overall beam power required to reproduce a certain lineshape can vary. Nevertheless, we reveal quite unexpected scalings of the resonances with different parameter settings.

6.2 Intensity and Detuning

In this section we investigate the lineshapes for different values of the effective Rabi frequency Ω_R for the Raman transitions. The Rabi frequency is proportional to the the product of the pump and the probe intensities divided by the detuning squared as shown in Section 3.1. In Section 6.2.1 we show the results for different intensities with fixed detuning. In Section 6.2.2 we investigate how the shape of the recoil-induced resonances varies with detuning.

The overall (peak-to-peak) signal should be directly proportional to the number of atoms the laser beams are interacting with. Unfortunately, the number of cold atoms provided in the cold atomic cloud by the magneto-optical trap is hard to measure. Moreover, it varies in time because the ion pump constantly removes atoms, and we have to refill the chamber from time to time (see Section 4.1). Therefore, we cannot compare the peak-to-peak signal between two measurements if their time difference is too large. Fortunately, the dominant observation in our investigations of the lineshapes at different effective Rabi frequencies is not related to the peak-to-peak signal.

6.2.1 Intensity Variations

All the measurements discussed in this section are taken at $\Delta_L = 2\pi\cdot(1.5 \pm 0.2)$ GHz detuning. First, we discuss the variations in the lineshape when the intensity in both beams is varied, while the ratio of the intensities is kept fixed. Then, we describe the effects of different intensity ratios.

The theory developed in Chapter 3 predicts no qualitative change in the lineshape when the effective Rabi frequency changes. Only the amplitude

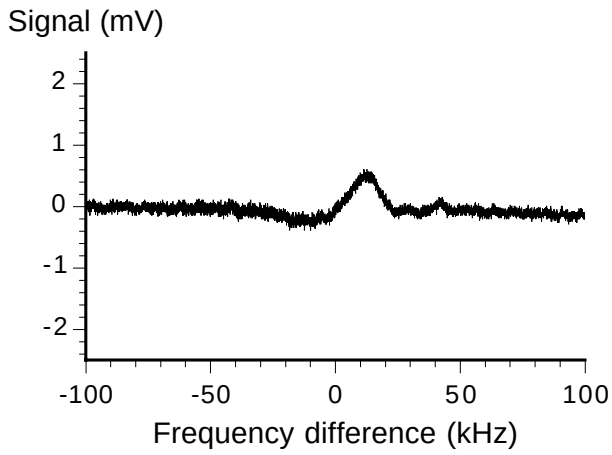

Figure 6.1: Lineshape at 1.5 GHz det., 0.9 mW pump, 0.03 mW probe. The first peak vanishes almost completely while the second peak is still quite pronounced. The overall signal-to-noise ratio is small at these low light powers.

should scale with the product of the intensities. This expectation has been supported by experimental observations for near-detuned pump and probe beams [3]. We observe a qualitatively different behavior in our experiments.

Figures 6.1 - 6.7 show the lineshapes for a ratio of pump to probe intensity of approximately 30. The signals are observed for pump intensities between 0.9 and 15 mW. Because the probe intensity varies only between 0.03 and 0.5 mW, the high frequency noise is relatively small. All lineshapes are obtained by averaging 10 measurements of the signal and the background and using the analysis procedure described in Section 5.4 to suppress the background and find the proper scaling of the graphs. At approximately 3 mW pump intensity, the lineshape is close to the derivative of a Gaussian as expected for all recoil-induced resonance experiments in our setup (see Fig. 6.4). Figure 6.5 shows the corresponding momentum distribution. It has a width of $(29 \pm 2)\ \hbar k$, which corresponds to a temperature of $(170 \pm 20)\ \mu$K. So, the

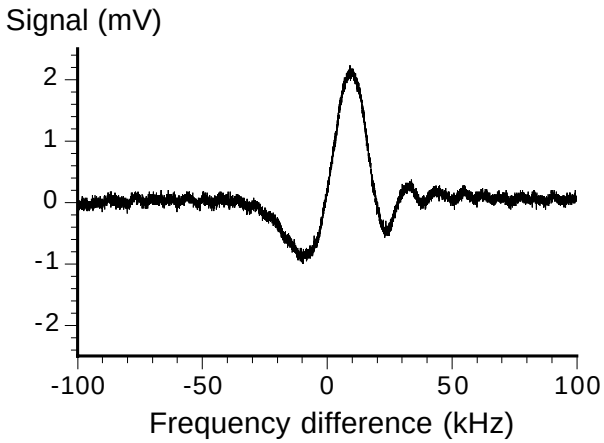

Figure 6.2: Lineshape at 1.5 GHz det., 1.5 mW pump, 0.05 mW probe. The second peak is much larger than the first peak at these powers. Furthermore, there are unpredicted, unexplained oscillations after the expected recoil-induced resonance.

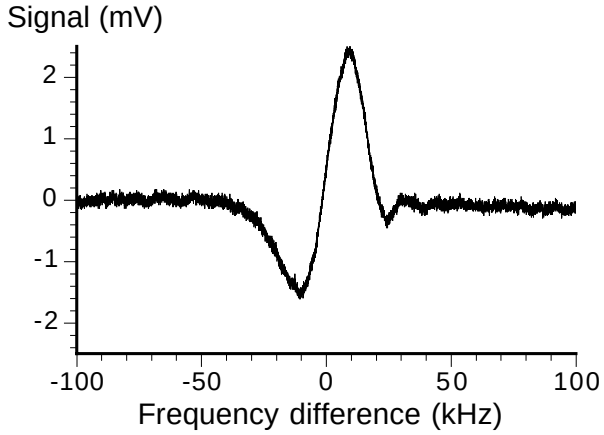

Figure 6.3: Lineshape at 1.5 GHz det., 2.25 mW pump, 0.075 mW probe. The signal level in the first peak drops below that of the second peak at these powers. There is almost no additional structure visible in the lineshape.

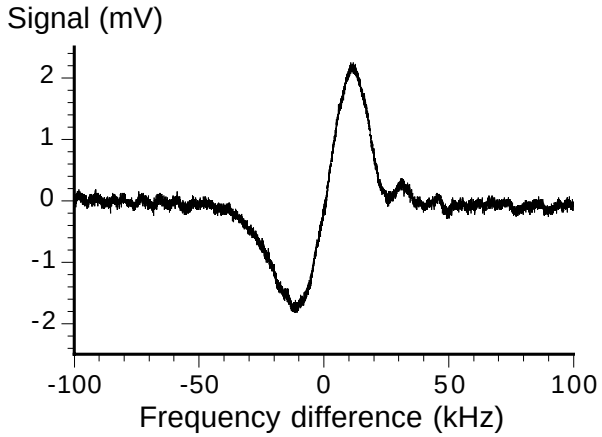

Figure 6.4: Lineshape at 1.5 GHz det., 3 mW pump, 0.1 mW probe. The lineshape is close to a derivative of a Gaussian. Fig. 6.5 shows the momentum distribution according to this signal.

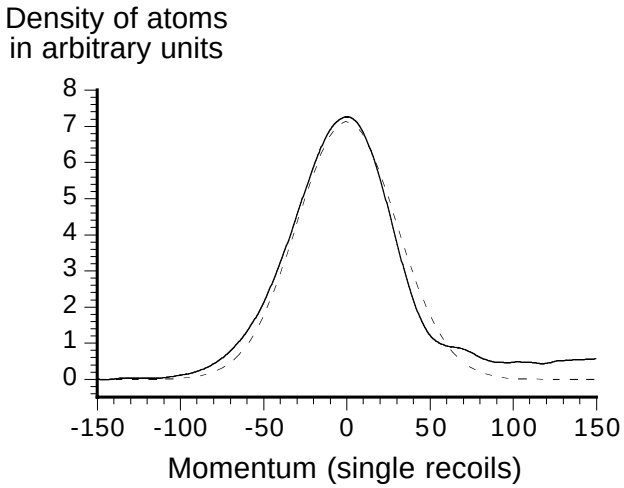

Figure 6.5: Integrated lineshape as measured at 1.5 GHz det., 3 mW pump, 0.1 mW probe. It is questionable if the almost Gaussian integrated data is really related to the momentum distribution according to the analysis presented in Section 5.4.

momentum distribution measured with the recoil-induced resonance method is much broader than the distribution measured by the time-of-flight method. The latter one typically varies around 14 recoils (Section 6.1). This difference in the width of the momentum distribution could have the same origin as the unexpected asymmetry of the time-of-flight momentum distribution. It is possible that we measure only the momentum distribution of the pushed (and therefore hotter) atoms with the recoil-induced resonance method. At different beam intensities, the temperature is expected to vary by a certain amount due to a difference in heating. However, we do not observe a significant broadening or narrowing of the Gaussian derivative, but a drastic deviation from the derivative of a Gaussian. At higher intensities, the first peak in the lineshape begins to dominate (see Figs. 6.6 and 6.7). It becomes more and more pronounced, while the second peak begins to disappear. Even the increase of the first peak does not scale with the square of the intensity as expected. The maximum negative voltage is not increasing quickly enough with increasing pump and probe intensities.

At this point, one can argue that the intensities leading to such disturbed lineshapes are too high, and we therefore are not in the perturbative regime described by the theory in Chapter 3. However, reducing the intensity in the pump and probe beams leads to the observation of the lineshapes shown in Figs. 6.1 - 6.3. The lineshapes also clearly deviate from the expected derivative of a Gaussian. In contrast to increasing the intensity decreasing it leads to a pronunciation of the second peak, while the first peak decreases almost as fast with decreasing intensity as it should. When we decrease the intensity further, the signal decays further and the mismatch between the two

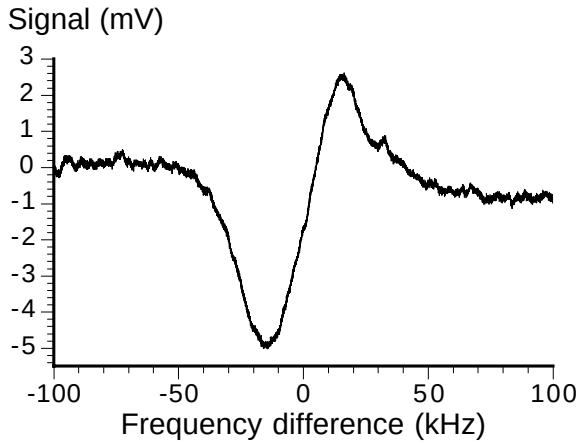

Figure 6.6: Lineshape at 1.5 GHz det., 9 mW pump, 0.3 mW probe. The second peak is not increasing according to the theoretical prediction with increasing beam powers. Therefore, the first peak dominates the whole lineshape.

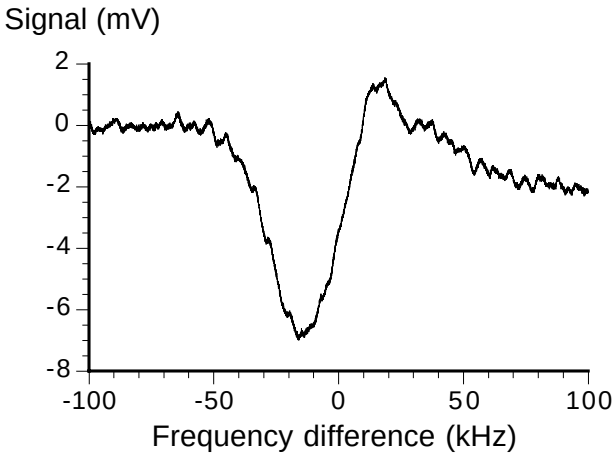

Figure 6.7: Lineshape at 1.5 GHz det., 15 mW pump, 0.5 mW probe. At the highest powers the background subtraction does not work reliably. There is no clear zero baseline in the signal. Nevertheless, the suppression of the second peak compared with the first one is striking.

peaks does not vanish until we lose the signal within the noise. Figure 6.1 shows the lineshapes at one of the lowest intensities, where it is still visible. It is also interesting that the lineshapes at low intensities show more structure than the expected two peaks. There are some thus far unexplained oscillations after the second peak (see, for example, Fig. 6.2). The variations of the lineshapes at different pump and probe intensities is even more unexpected than the puzzles discussed before. These variations make the meaning of the evaluated temperatures questionable (Chapter 7).

Integrating all the lineshapes that are not close to a derivative of a Gaussian in order to extract the momentum distribution yields meaningless results. The integrated signals of these lineshapes do not even have a well-defined zero baseline. Therefore, there are no physical momentum distributions that would give rise to these lineshapes, and thus it is clear that the theory does not hold for our experiment. Various possible reasons are discussed in Chapter 7.

As further measurements show, the observed qualitative change in the lineshapes is not a special feature of the large ratio of pump intensity to probe intensity but quite universal. At different ratios we observe exactly the same pronunciation of the first peak for higher intensities and of the second peak for lower intensities. Figures 6.8 and 6.9 show an example of a pump to probe intensity ratio of 4. We can observe the same variations in the lineshapes down to a ratio of one. Beyond the ratio of one the signal-to-noise in the observed lineshapes becomes too poor to make sensible measurements.

Naturally, the question arises if the form of the measured lineshapes

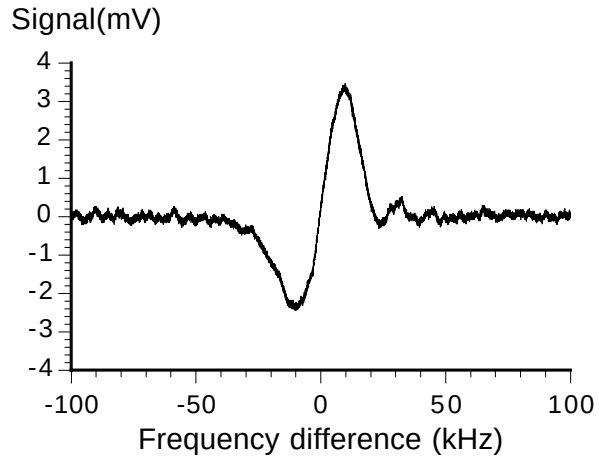

Figure 6.8: Lineshape at 1.5 GHz det., 1.2 mW pump, 0.3 mW probe. In contrast to the previous graph, the pump to probe intensity ratio is only four. However, the graph is similar to the graph at a much higher pump to probe intensity ratio shown in Fig. 6.3.

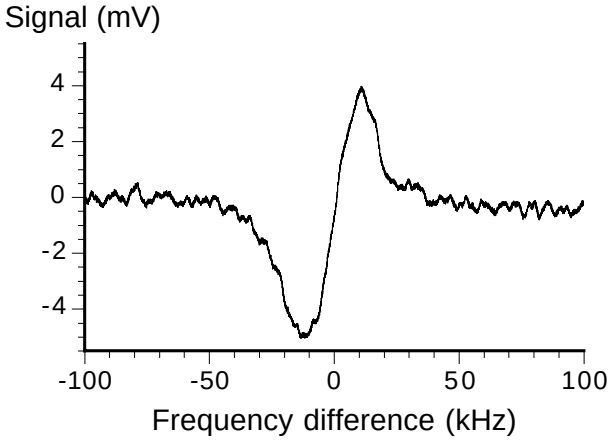

Figure 6.9: Lineshape at 1.5 GHz det., 2.4 mW pump, 0.6 mW probe. The pump to probe power ratio is four. The graph is similar to the graph shown in Fig. 6.6.

depends on each intensity (pump and probe) or only on the product of both intensities, as suggested by the theoretical treatment. This question is hard to answer for several reasons. First, there are drifts in the overall intensity and the detuning during the experiments because of the instability of the Ti:sapphire laser (up to 10%). Second, realignment of the laser beams on the atoms does not qualitatively change our observations on variations in the lineshapes, but it can change the overall intensity where a certain lineshape is observed. Finally, it is hard to decide which intensities lead to equivalent lineshapes for different intensity ratios. These problems lead to large deviations in the observed product of the beam powers. For example, almost Gaussian lineshapes are observed from 0.2 to 0.8 $(\mathrm{mW})^2$ (most likely due to realignment effects). However, the fluctuations appear to be rather random and do not show a clear deviation from the expected scaling with the effective Rabi frequency Ω_R.

6.2.2 Detuning Variations

Because of the drifts in the overall frequency of the Ti:sapphire laser and its linewidth of 10 MHz, our setup is not suitable for working in a near-detuned regime. Therefore, it is not possible to reproduce the results in [2,3]. At a detuning beyond $\Delta_\mathrm{L} = 2\pi{\cdot}750$ MHz, the observed lineshapes follow the discussion in Section 6.2.1. The same series of graphs as shown in Fig. 6.1 to Fig. 6.7 can be reproduced qualitatively at each detuning up to $\Delta_\mathrm{L} = 2\pi{\cdot}6$ GHz. Larger detunings require more intensity to measure a qualitatively equivalent lineshape. Therefore, the signal-to-noise ratio drops significantly for larger detunings.

As in the case of different intensity ratios of the pump and probe beams,

there is no significant deviation from the expected dependence of the lineshapes solely on the effective Rabi frequency. All measurements performed at one day without any necessary realignments show that the lineshapes that are most similar to a derivative of a Gaussian occur at the same Ω_{R}, within 20%. However, in addition to the problems with analyzing our data (discussed in Section 6.2.1) these measurements were done without averaging over multiple runs of the experiment and without taking background measurements. In other words, only raw data as shown in Section 5.4 is available for the analysis. More time-consuming averaged measurements must be done to find a systematic deviation that might be hidden in our uncertainties.

6.3 Polarization

All the measurements presented so far were performed with parallel linear polarizations of the pump and probe beams. We also performed measurements with other polarization configurations, which we discuss in this section. As for the investigations at different detunings, only the raw data is available for the analysis of our observations.

As discussed in Section 3.3.2, the theory for polarization configurations, in which pump and probe do not have parallel, linear polarizations, becomes involved. Because the necessary calculations for predictions are beyond the scope of this thesis, we do not compare our experimental results to the theory.

6.3.1 Different Pump and Probe Polarizations

One possible different configuration is to keep the polarization of both beams linear but rotate the probe polarization with respect to the pump polarization. We observe that the recoil-induced resonance lineshape disappears completely if the polarization directions of the pump and the probe are perpendicular. While increasing the angle between the two polarization directions from 0 to 90° the signal decreases until it vanishes completely within the noise. The different coupling of the probe beam to pump beams with different polarizations suggests that a polarization spectroscopy setup can be used (Section 6.3.2).

We investigated another possible configuration, namely using circularly polarized light for the pump beam while keeping the probe beam linearly polarized. We do not observe significant differences between these measurements and the measurements presented in Section 6.2.1. The lineshapes that are observed using circularly polarized pump light are similar in shape and peak-to-peak signal to the lineshapes observed with identical experimental conditions but linearly polarized pump light.

6.3.2 Polarization Spectroscopy

In polarization spectroscopy [16] , one does not observe the direct intensity change in a laser beam, but one detects the rotation of the polarization direction of linearly polarized light. The big advantage of such a method is that the measured signal does not have a large background. The principles of polarization spectroscopy are most easily explained using the example of the polarization spectroscopy setup we used in our experiment.

The pump and the probe beams are linearly polarized at 45° with respect to each other. As described in Section 5.1.1, this can be accomplished by appropriately inserting the half-wave plate in front of the vacuum chamber. After the chamber, a crossed polarizer is inserted into the beam path. In other words, almost no light impinges on the photodiode measuring the probe intensity after the chamber. To optimize the extinction ratio of the polarizer, a second polarizer can be included in front of the chamber in order to filter out all the light that is not properly polarized in the specified direction. Our polarizers can provide an extinction ratio of 3×10^{-4}. Therefore, all our background and power-induced noise problems should be automatically solved in this configuration. Our subtraction scheme is obsolete and not used.

Polarization spectroscopy relies on the fact that the polarization direction of the probe beam is changed during the measurement. A simple model would suggest that we can think of the probe beam (polarized at 45° with respect to the pump) as a linear combination of light with parallel and perpendicular polarization with respect to the pump. Because the coupling between perpendicularly polarized beams is zero, the intensity variation in the parallel component of the light should yield a slight rotation of the polarization direction during the recoil-induced resonance measurement. Therefore, the polarizer after the chamber does not extinguish all the incoming light any more, and a signal should be visible. The absolute value of the signal cannot be expected to be as big as in a direct power measurement in this model because of the geometry of the setup. However, the advantage of eliminating the background cannot be overemphasized.

In contrast to this model, there is no experimental evidence of any rotation of the direction of the pump beam polarization. Each attempt to measure any resonant lineshape in the polarization spectroscopy setup has failed so far. There is no photodiode signal at all during the whole sweep. We also changed the pump beam configuration and used a circularly polarized pump beam. However, this has not resulted in any visible beam shape either.

Chapter 7

Conclusions

This thesis describes the realization of recoil-induced resonance experiments and the first measurements using our setup. The data show that we observed narrow, resonant structures that are similar to the predicted lineshapes. However, more work has to be done to make recoil-induced resonances useful for temperature measurements or even velocimetry of cold cesium atoms.

First of all, most of the lineshapes do not allow for extracting a momentum distribution at all. The qualitative change in the lineshape with different beam intensities gives obviously meaningless results for the corresponding momentum distributions. Therefore, one has to be careful about the interpretation of a "momentum distribution" as shown in Fig. 6.5. The justification for interpreting the integrated lineshape as the momentum distribution of the atoms is the theory developed in Chapter 3 or by Guo *et al.* [1], but it seems to fail to predict the lineshapes in most of our experiments. Furthermore, we can only observe lineshapes in a clearly destructive regime, in which the momentum distribution of the initial thermal cloud is altered significantly as observed in the time-of-flight measurements.

The theory has successfully predicted results that are obtained at dif-

ferent experimental parameters [2,3]. Therefore, the question arises why it fails to predict our results.

There are certainly different possible explanations. We cannot exclude the possibility that our experimental setup includes a systematic error that is responsible for the qualitative change in the lineshapes. In this case, different experimental setups should yield qualitatively different results. However, to our knowledge, there are no experimental results that are obtained close to our experimental parameters.

If there is no principal systematic error involved, either the recoil-induced resonances are different from the theoretical predictions in Chapter 3, or there is another resonant structure that is superimposed with the recoil-induced resonance signal. In either case, the question arises which parameter makes us leave the region where the theory is valid. In comparison with the experiments in Paris [2,3] we use several different parameters.

First of all, our detuning is 50 times larger then in the previous measurements. As discussed in Section 3.3.2, the coupling of the Raman transitions to all the hyperfine sublevels of the excited state could lead to complications.

Second, even the smallest effective Rabi frequencies that we use are higher than those reported in [2,3]. However, at low beam powers the product of the beam intensities divided by the detuning squared (which is proportional to the effective Rabi frequency) can be estimated to be 0.048 $(\mathrm{W/cm^2})^2\ \mathrm{GHz}^{-2}$ and is therefore at least comparable to the other group's values [2,3] (up to 0.05 $(\mathrm{W/cm^2})^2\ \mathrm{GHz}^{-2}$). However, if our estimate is wrong and too small, we could certainly be in a regime where the perturbative analysis fails. As discussed in

Section 6.1, for example, our beam waist at the atoms could be much smaller than we think it is. We cannot exclude the possibility that the lineshapes at much smaller Rabi frequencies follow the theoretical prediction. To investigate smaller Rabi frequencies, a more sophisticated measurement technique with a much better signal-to-noise ratio must be implemented. One possibility might be to make use of FM spectroscopy techniques [17].

Third, our sweep rate is almost 6 times larger than in the other experiments [2,3]. Therefore, the dynamical problems discussed in Section 3.3.3 could make the theory invalid at our parameters. To investigate this, a measurement technique with fewer noise and background problems, such as FM spectroscopy, might be helpful as well because it could allow for experiments at smaller sweep rates without being concerned about the signal-to-noise ratio.

Finally, the repump laser is incident on the atoms during the interaction, and there is a nonzero magnetic field because it is still ringing down (see Section 5.3). Both effects would complicate a more sophisticated theoretical analysis and could be responsible for the observation of the disturbed lineshapes.

Another question is why our polarization spectroscopy setup does not work at all. In a different experimental setup, recoil-induced resonances are predicted to rotate the polarization direction of the probe beam [18]. Again, we cannot be sure if only our poor noise suppression is responsible for the missing signal or if there is a physical reason that prohibits the rotation of the polarization for our setup. For example, the magnetic field is still ringing down and has not completely vanished at the time of our experiment (see Section

5.3). Therefore, Zeeman shifts of the magnetic sublevels might prohibit an otherwise possible rotation of the polarization direction.

Finally, we conclude that velocimetry with our current setup does not seem to be possible. Nevertheless, we are confident that a more sophisticated experimental setup and a more specific theoretical analysis for our experimental conditions will be helpful to reach the final goal of a spectroscopic, nondestructive velocimetry method. The first step, measuring recoil-induced resonances, has been accomplished.

Appendices

Appendix A

Cesium Hyperfine Structure

Figure A.1 shows the hyperfine structure of the cesium D_2 line. The energy separations of the levels are not shown to scale. The wavelength ($\approx$ 852 nm) of all the lasers that we use in our cesium experiments is determined by the energy separation of the $6\,^2S_{1/2}$ and $6\,^2P_{3/2}$ states.

The hyperfine splitting of the ground state (9.19262317700 GHz) defines the length of one second and is therefore exact. The splittings between the hyperfine levels of the excited state are much smaller ($\approx 150-250$ MHz). For a laser that is detuned several GHz to the red from the $F = 4$ to $F' = 5$ transition the excited states therefore are approximately degenerate. The Ti:sapphire laser used for the recoil-induced resonance beams is one example of such a laser. The difference in detuning of several hundred MHz compared with several GHz is simply unimportant. Nevertheless, transitions including the $F = 3$ state are still much further detuned and therefore much less probable.

The cooling and trapping laser, which is less intense and tuned closely to the $F = 4$ to $F' = 5$ transitions, almost only drives this transition because at low intensities its detuning with respect to the other transitions (200 MHz or more) has to be considered large.

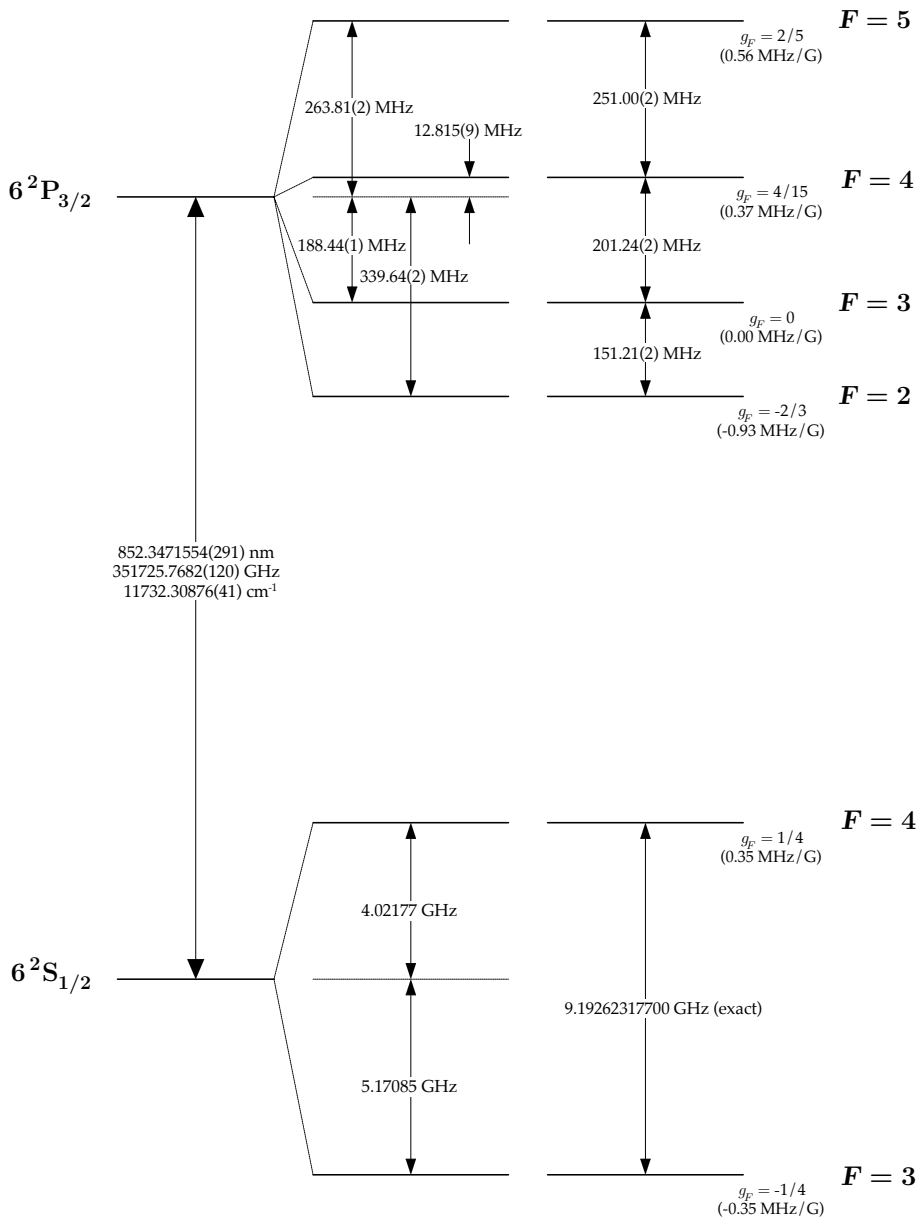

Figure A.1: Cesium hyperfine structure, with frequency splittings between the hyperfine energy levels. The Landé g-factors g_F for each level are also given, with the corresponding Zeeman splittings between adjacent magnetic sublevels. (Graphics reproduced from [15])

Appendix B

Acousto-Optic Modulators

Acousto-optic modulators (see also [19]) rely on the Bragg scattering of light from sound waves. A traveling acoustic wave of frequency Ω is created in dense flint glass using Lithium Niobate piezoelectric transducers by applying an RF input at this frequency. This sound wave leads to a variation in the density of the medium with a periodicity of $\Lambda = 2\pi v/\Omega$, where v is the sound speed in the medium. Associated with the density variation is a variation in the dielectric constant and therefore in the index of refraction. If the usual Bragg condition

$$\lambda = 2\Lambda \sin\theta, \tag{B.1}$$

where λ is the wavelength of the light and θ is the incident angle (see Fig. B.1), is fulfilled, constructive interference of the light waves scattered by the different acoustic wavefronts results in a significant amount of scattered light intensity. The scattered beam leaves the modulator at 2θ relative to the incoming beam. Therefore, the AOM can be used as a light deflector in order to have electronic control over the propagation direction of the light. The Bragg condition can alternatively be written as $\vec{k}_2 = \vec{k}_1 \pm \vec{q}$, where $\vec{q}$ is the wave vector of the acoustic wave and $\vec{k}_1, \vec{k}_2$ are the wave vectors of the light (see Fig. B.1). The

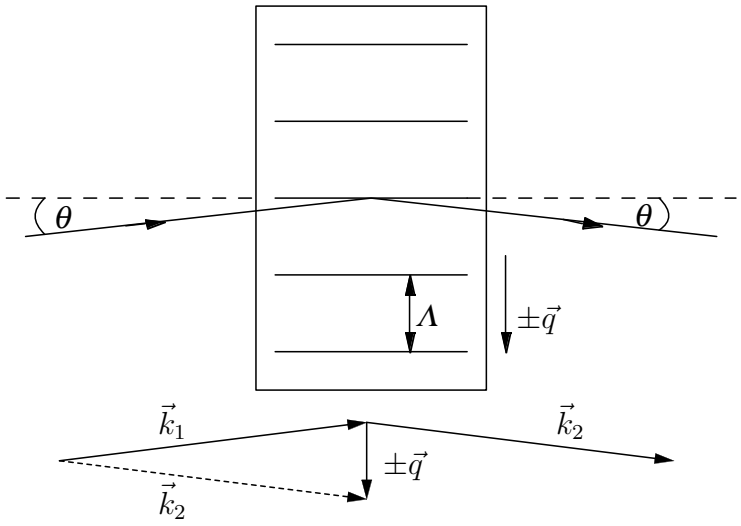

Figure B.1: Principle of an acousto-optic modulator

sign depends on the direction of propagation of the acoustic wave relative to the incoming beam.

One extremely useful property of an AOM in many experimental applications is that the frequency of the scattered beam ω_2 is shifted to

$$\omega_2 = \omega_1 \pm \Omega, \tag{B.2}$$

where ω_1 is the frequency of the incoming light. This results from the fact that the acoustic wave moves with the sound speed of the medium and therefore Doppler shifts the frequency of the light. The sign again depends on the propagation direction of the sound wave relative to the light. A diffracted beam with a frequency shifted down is called the -1 order, while the one shifted up is referred to as the +1 order. Naturally, only one of them is produced in a certain alignment. In other words, within certain limits (usually 10-20% to both sides

of the AOM's center frequency), the RF input frequency directly controls the frequency shift and therefore the frequency of the outgoing deflected beam.

The percentage of intensity in the scattered beam depends on the amplitude of the acoustic wave, which can be controlled by the amplitude of the RF input. For optimum alignment one can show that this percentage of light in the first order is given by

$$\eta = \frac{I_1}{I} = \sin^2\Big(c\Big(\frac{P_a}{\lambda^2}\Big)^{1/2}\Big), \tag{B.3}$$

where c is a constant depending on the geometry of the sound wave and the material of the crystal, and P_a is the power in the acoustic wave. In other words, an AOM allows for direct control of the light intensity in the diffracted beam. Small misalignments of the incident beam decrease the efficiency of the modulator.

Equation B.1 shows that the deflection angle 2θ depends on the frequency of the acoustic wave. Changing the frequency (for example in a sweep) therefore changes the propagation direction of the light. In experiments where precise alignment and a variable frequency is needed this is a big disadvantage. Fortunately, one can easily overcome this problem by double-passing an AOM. The setup and alignment for a double pass are described in Sections 5.1.1 and 5.1.2.

Bibliography

[1] J. Guo and P.R. Berman, *Recoil-induced resonances in nonlinear spectroscopy*, *Phys. Rev. A* **46**, 1426 (1992).

[2] J.-Y. Courtois, G. Grynberg, B. Lounis, and P. Verkerk, *Recoil-Induced Resonances in Cesium: An Atomic Analog to the Free-Electron Laser*, *Phys. Rev. Letters* **72**, 3017 (1994).

[3] D.R. Meacher, D. Boiron, H. Metcalf, C. Salomon, and G. Grynberg, *Method for velocimetry of cold atoms*, *Phys. Rev. A* **50**, R1992 (1994).

[4] C. Cohen-Tannoudji, J. Dupont-Roc, and Gilbert Grynberg, *Atom-Photon Interactions, Basic Processes and Applications*, (John Wiley & Sons, New York, 1998).

[5] C. Cohen-Tannoudji, *Manipulating atoms with photons*, *Rev. Mod. Phys.* **70**, 707 (1998).

[6] S. Chu, *The manipulation of neutral particles Rev. Mod. Phys.* **70**, 685 (1998).

[7] W.D. Phillips, *Laser cooling and trapping of neutral atoms*, *Rev. Mod. Phys.* **70**, 721 (1998).

[8] J. Dalibard, and C. Cohen-Tannoudji, *Laser cooling below the Doppler limit by polarization gradients: simple theoretical models*, *J. Opt. Soc. Am. B* **6**, 2023 (1989).

[9] D.A. Steck, *Atomic Motion in a Standing Wave of Far-Detuned Light*, available on-line at `http://www.ph.utexas.edu/ quantenopt.`

[10] B.H. Bransden, and C.J. Joachain, *Physics of Atoms and Molecules*, (John Wiley & Sons, New York, 1983).

[11] J. Guo, and P.R. Berman, *Recoil-induced resonances in pump-probe spectroscopy including effects of level degeneracy*, *Phys. Rev. A* **47**, 4128 (1993).

[12] B.G. Klappauf, *Experimental Studies of Quantum Chaos with Trapped Cesium*, Ph.D. Dissertation, University of Texas at Austin (1998).

[13] J.C. Robinson, *Atom Optics, A New Testing Ground for Quantum Chaos*, Ph.D. Dissertation, University of Texas at Austin (1995).

[14] J.T. Verdeyen, *Laser electronics*, 3rd edition, (Prentice Hall, Englewood Cliffs, 1995).

[15] D.A. Steck, *Cesium D_2 Line Data*, available on-line at `http://www.ph.utexas.edu/ quantenopt.`

[16] W. Demtröder, *Laser Spectroscopy*, 2nd enlarged edition, (Springer, Berlin, 1996).

[17] G.C. Bjorklund, and M.D.Levenson, *Frequency Modulation (FM) spectroscopy*, *Appl. Phys. B* **32**, 145 (1983).

[18] B. Dubetsky, and P.R. Berman, *Recoil-induced optical Faraday rotation*, *Phys. Rev. A* **52**, R2519 (1995).

[19] R.W. Boyd, *Nonlinear Optics*, (Academic Press, San Diego, 1992).

Vita

Alexander Mück was born on March 04, 1975 in Fulda, Germany as the son of Franz Mück and Hiltrud Mück. He received his Abitur from the Freiherr-vom-Stein-Schule in Fulda in 1994. The next twelve month he spent in mandatory military service. He started studying physics at the Bayerische Julius Maximilians Universität Würzburg in November of 1995. After receiving his Vordiplom in August 1997 and studying physics for one additional year in Würzburg, he entered the graduate school at the University of Texas at Austin in August 1998. Since 1996 he has been a scholar of the Studienstiftung des deutschen Volkes (German National Merit Foundation).

Permanent address: Am Hofgut 2, 36100 Petersberg, Germany

This thesis was typeset with LaTeX[‡] by the author.

[‡]LaTeX is a document preparation system developed by Leslie Lamport as a special version of Donald Knuth's TeX Program.